




## REVIEW ARTICLE

## Component leaching of water oxidation electrocatalysts

Gao Chen<sup>1</sup>  | Yanping Zhu<sup>2</sup> | Sixuan She<sup>3</sup> | Zezhou Lin<sup>3</sup> |  
Hainan Sun<sup>4</sup>  | Haitao Huang<sup>3</sup> 

<sup>1</sup>Jiangsu Key Laboratory of New Energy Devices and Interface Science (Nanjing University of Information Science and Technology), School of Chemistry and Materials Science, Nanjing University of Information Science and Technology, Nanjing, the People's Republic of China

<sup>2</sup>College of Materials Science and Technology, Nanjing University of Aeronautics and Astronautics, Nanjing, the People's Republic of China

<sup>3</sup>Department of Applied Physics and Research Institute for Smart Energy, The Hong Kong Polytechnic University, Hong Kong, the People's Republic of China

<sup>4</sup>School of Chemistry and Chemical Engineering, Nantong University, Nantong, the People's Republic of China

**Correspondence**

Yanping Zhu, College of Materials Science and Technology, Nanjing University of Aeronautics and Astronautics, Nanjing 210016 the People's Republic of China.  
Email: [yanping.zhu@nuaa.edu.cn](mailto:yanping.zhu@nuaa.edu.cn)

Haitao Huang, Department of Applied Physics and Research Institute for Smart Energy, The Hong Kong Polytechnic University, Hong Kong, the People's Republic of China.  
Email: [aphhuang@polyu.edu.hk](mailto:aphhuang@polyu.edu.hk)

**Funding information**

the Program for Jiangsu Specially-Appointed Professors; the Startup Foundation for Introducing Talent of NUIST, Grant/Award Number: 2024R078; the Hong Kong Polytechnic University, Grant/Award Numbers: 1-WZ5L, Q-CDBG, 1-ZE2F

**Abstract**

Most electrocatalysts are known to experience structural change during the oxygen evolution reaction (OER) process. Considerable endeavors have been dedicated thus far to comprehending the catalytic process and uncovering the underlying mechanism. During the dynamic evolution of catalyst structure, component leaching of electrocatalysts is the most common phenomenon. This article offers a concise overview of recent findings and developments related to the leaching phenomena in the OER process in terms of fundamental understanding of leaching, advanced characterization techniques used to investigate leaching, leaching of inactive components, and leaching of active components. Leaching behaviors and the induced effects in various kinds of OER catalysts are discussed, progress in manipulating leaching amount/degree toward a tunable surface evolution is spotlighted, and finally, three representative types of structure transformations induced by leaching metastable species in OER condition are proposed. By understanding the process of component leaching in the OER, it will provide more guidance for the rational design of superior electrocatalysts.

**KEYWORDS**

leaching, oxygen evolution reaction, reconstruction, water oxidation

## 1 | INTRODUCTION

The escalating worldwide energy demand and environmental concerns necessitate the exploration and advancement of alternate and sustainable energy sources as substitutes for conventional fossil fuels. Hydrogen ( $H_2$ ) is regarded as one of the cleanest energy carriers, primarily because of zero-carbon emissions.<sup>1–4</sup> Electrochemical water splitting, powered by renewable electricity, is considered an environmentally friendly and enduring method for generating  $H_2$ . Water splitting involves the oxygen evolution reaction (OER) occurring on the anode and hydrogen evolution reaction (HER) occurring on the cathode. Because of the involvement of four-electron transfer in the OER, it is widely accepted that the OER is more complex and slower compared to the HER, which involves only two-electron transfer.<sup>5–10</sup> Hence, it is imperative to create highly efficient OER catalysts that exhibit exceptional activity and long-lasting stability in order to enhance the overall efficiency of water splitting.

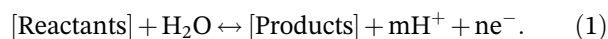
Significant progress has been achieved in the field of material exploration to enhance the efficiency of OER. Transition-metal-based materials, including alloys, hydroxides, oxides, chalcogenides, phosphides, nitrides, carbides, borides, and single-atom materials, have been extensively studied as viable alternatives for alkaline OER.<sup>11–15</sup> For the OER in acidic conditions, the electrocatalysts primarily consist of precious elements Ir or Ru. This is because most transition elements are unable to maintain stability in acidic environments.<sup>16,17</sup> In addition to the notable advancements in material exploration, it has been generally noted that the surface structure of the OER catalyst undergoes instability throughout the OER process, hence challenging the conventional understanding of a “catalyst”.<sup>18–25</sup>

To better understand the fundamental process of OER catalysis, much research has been conducted to investigate how catalysts evolve in OER conditions. One of the most prevalent occurrences is the leaching of components from the catalysts. Electrochemical leaching is the scientific term used to describe the process in which a soluble component is separated or extracted from its carrier substance and transferred into an electrolyte. When subjected to an OER potential, the metastable species, which possess fragile bonds in their initial structure and are soluble in the electrolyte, can readily detach from the crystal lattice and dissolve into the electrolyte, resulting in the disruption of the initial structure, the generation of defects, and the exposing of more solid–liquid interface. Furthermore, the species that have been leached out can be re-deposited by forming a new amorphous layer that might potentially exhibit higher OER activity.

This review paper presents a comprehensive summary of the leaching of components from electrocatalysts during electrochemical water oxidation. After briefly introducing the origin of element leaching from the thermodynamic point of view, applications of advanced characterization techniques in analyzing the change of electrocatalysts induced by component leaching are generalized. We classify the leaching phenomena during OER into two categories: inactive and active component leaching. The leaching behaviors as well as the induced effects of several categories of OER catalysts with distinct structures and properties are discussed in detail, after which three representative types of structure transformations induced by leaching metastable species are summed up. Finally, we provide an outlook on possible avenues for expanding our knowledge of component leaching in electrochemical reactions and rational design of advanced electrocatalysts.

## 2 | FUNDAMENTAL UNDERSTANDING OF LEACHING

Leaching is the wastage of material by chemical action of its environment. Aqueous leaching is the oxidation of an element via an electrochemical reaction with water and its dissolved compounds. The Pourbaix diagrams (potential-pH diagrams) provide a precise knowledge of element leaching in aqueous systems based on equilibrium thermodynamics.<sup>26</sup> Pourbaix diagrams allow one to forecast, from a thermodynamic point of view, the equilibrium states of a given element in the presence of water at a certain potential.<sup>27–30</sup> The construction of the Pourbaix diagram involves determining the stable domains by considering all potential equilibrium redox reactions within the relevant chemical species.<sup>28–30</sup> The given redox reaction occurs in an aqueous solution at a specific pH ( $-\log [H^+]$ ) and potential ( $E$ )<sup>28</sup>:



The Nernst equation allows us to establish a relationship between the Gibbs free energy change ( $\Delta G_{\text{rxn}}$ ) of this reaction and  $E$  at equilibrium<sup>28</sup>:

$$\begin{aligned} -nFE &= \Delta G_{\text{rxn}} \\ &= \Delta G_{\text{rxn}}^0 + 2.303 \times RT \times \log \frac{a_{\text{reactants}}}{a_{\text{products}}} - 2.303 \\ &\quad \times RT \times m \times \text{pH}. \end{aligned} \quad (2)$$

The variables in the equation are as follows:  $\Delta G_{\text{rxn}}^0$  represents the change of Gibbs free energy of the reaction under standard conditions,  $F$  represents the Faraday

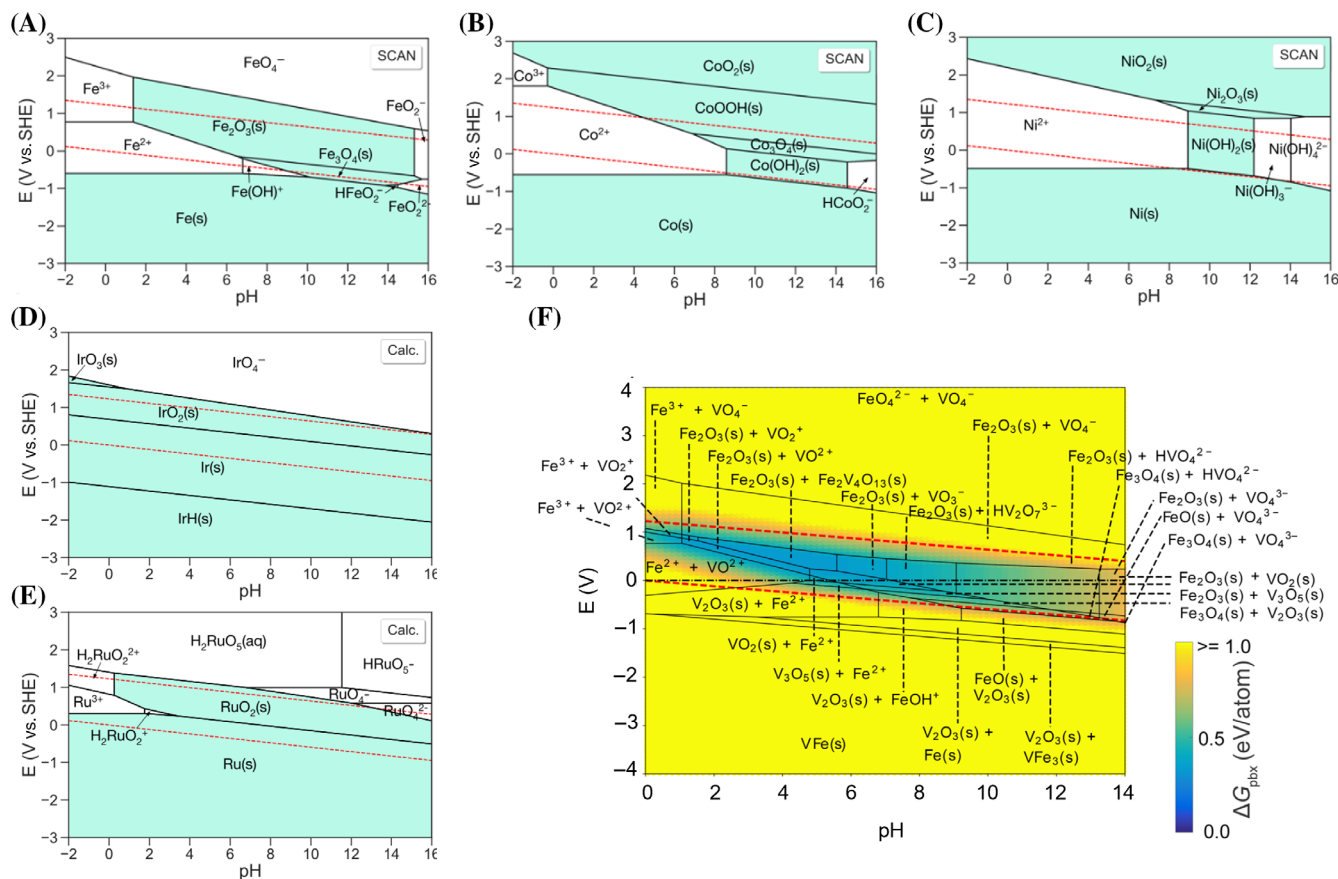


**FIGURE 1** Pourbaix diagram of (A) Fe, (B) Co, (C) Ni, (D) Ir, and (E) Ru. Reproduced under a CC-BY License.<sup>30</sup> Copyright 2020, the Authors. Published by Nature Publishing Group. (F) Computationally predicted Pourbaix diagram of the Fe-V-O-H system. Reproduced with permission.<sup>31</sup> Copyright 2017, American Chemical Society.

constant,  $R$  represents the gas constant,  $T$  represents the temperature, and  $a$  represents the activity.

Figure 1A–E presents the Pourbaix diagrams for several prevalent active elements (Fe, Co, Ni, Ir, and Ru) pertinent to water oxidation processes. Utilizing Ruthenium (Ru) as a case study to elucidate the Pourbaix diagram, it is observed that under highly alkaline conditions conducive to the OER, Ru transitions into soluble species, specifically  $\text{RuO}_4^-/\text{RuO}_4^{2-}$ , which subsequently transforms into  $\text{HRuO}_5^-$  species at elevated potentials. In both neutral and acidic OER environments,  $\text{H}_2\text{RuO}_5$  is formed, existing as a soluble species. Remarkably,  $\text{RuO}_2$  is stable over a narrow potential range, enabling it to act as a catalyst for the OER.

Pourbaix diagram is a powerful tool to assess the stability of electrocatalysts under different potential and pH settings in aqueous environments. Singh et al. introduced the concept that the stability of a catalyst in aqueous can be measured by calculating the difference in Gibbs free energy ( $\Delta G_{\text{pbx}}$ ) between the catalyst and the stable regions on the Pourbaix diagram. This calculation takes into account the pH and potential, and is based on

the difference in chemical potential between the catalyst and the stable chemical species.<sup>31</sup> Generally, a substance that has a  $\Delta G_{\text{pbx}}$  value of 0 is considered to be the most stable and will be shown on the Pourbaix diagram. The greater the magnitude of  $\Delta G_{\text{pbx}}$ , the less stable the substance in aqueous solution. Figure 1F illustrates the Pourbaix diagram of the Fe-V-O-H system with a 1:1 composition of Fe and V in an unlimited supply of water. The  $\Delta G_{\text{pbx}}$  associated with the stable zones in the Pourbaix diagram provides an estimate of the instability of  $\text{FeVO}_4$ . The smallest value of  $\Delta G_{\text{pbx}}$ , which is 0.34 eV/atom, is particularly found at pH = 1.63 and  $E = 0.85$  V. At these conditions, a phase transformation to  $\text{Fe}_2\text{V}_4\text{O}_{13}$  and  $\text{Fe}_2\text{O}_3$  is projected to occur. Following a thorough examination of 20 different materials, it was shown that materials with a predicted  $\Delta G_{\text{pbx}}$  of up to 0.5 eV/atom can potentially maintain stability in water-based environments, contingent upon the characteristics of their projected decomposition products. Leaching is likely to occur when there is a significant driving force for decomposition ( $>0.5$  eV/atom) and/or when breakdown solely results in the formation of aqueous species.

### 3 | ADVANCED CHARACTERIZATION TECHNIQUES TO STUDY LEACHING

The component leaching typically brings changes in electrocatalysts under OER condition, such as changes in morphology, structure, composition, electronic configuration, and so on. The well-developed spectroscopy and microscopy techniques, particularly the advancements in *in situ/operando* means, enables the analysis of the leaching phenomenon in OER process. In this section, a variety of physicochemical characterization techniques for studying component leaching of OER catalysts are discussed.

#### 3.1 | Microscopy techniques

Ion leaching of an electrocatalyst during OER catalysis usually causes the change of morphology, which can be studied by various kinds of microscopic analysis techniques. Scanning and transmission electron microscopies

(SEM and TEM) are indispensable instruments for microstructure analysis, offering information on size, shape, crystallinity as well as composition of the sample.<sup>32–34</sup> For example, Over et al. reported catalytic stability experiments on the  $\text{IrO}_2\text{--RuO}_2$  model electrodes.<sup>35</sup> The *ex situ* SEM image revealed the occurrence of pitting corrosion at the grain boundaries of the surface, caused by the leaching of Ir under anodic potential (Figure 2A). In another representative work conducted by Chung's group, by using atomic-column-resolved STEM, they demonstrated the surface variation of  $\text{AlIrO}_3$  (A = alkaline-earth).<sup>36</sup> Figure 2B illustrates the structural changes during anodic cyclic voltammetry, using a sequence of high-angle annular dark-field (HAADF) photographs. Evidently, the  $\text{SrIrO}_3$  structure readily undergoes collapse, resulting in the formation of nanoscale crystallites in the surface area. In addition to these images, two sets of energy-dispersive spectroscopy (EDS) composition maps clearly show that Sr is released in substantial amounts, resulting in the formation of a surface layer composed of nano-crystallites based on Ir-oxide (Figure 2C). Recently, our group observed the surface evolution of  $\text{AgNbO}_3$  perovskite under OER potentials by using

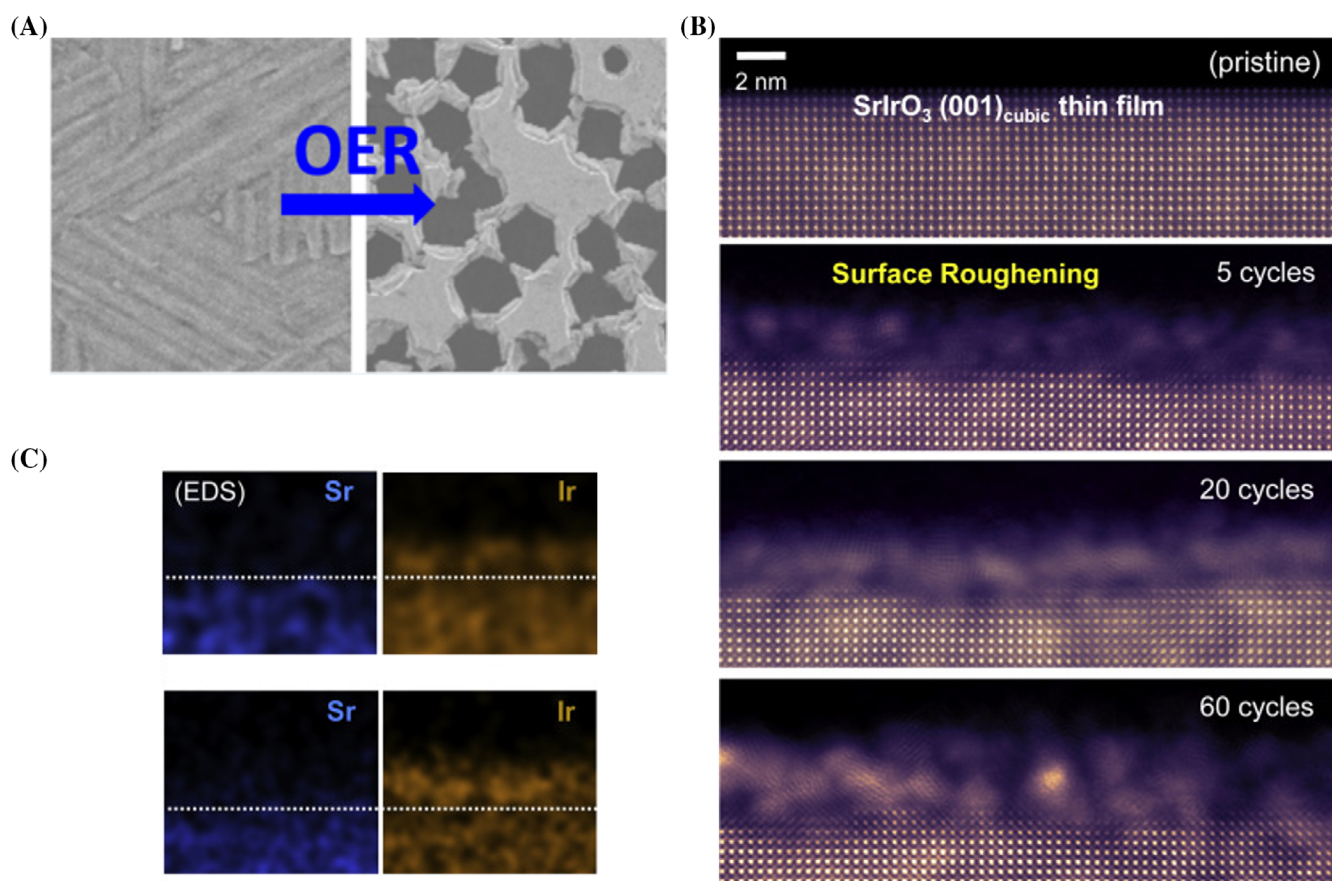


**FIGURE 2** (A) SEM images revealing the corrosion process of  $\text{IrO}_2$  in an acidic environment. Reproduced with permission.<sup>35</sup> Copyright 2019, American Chemical Society. (B) HAADF images of the surface structural evolution during the OER. Reproduced with permission.<sup>36</sup> Copyright 2019, Elsevier Inc.



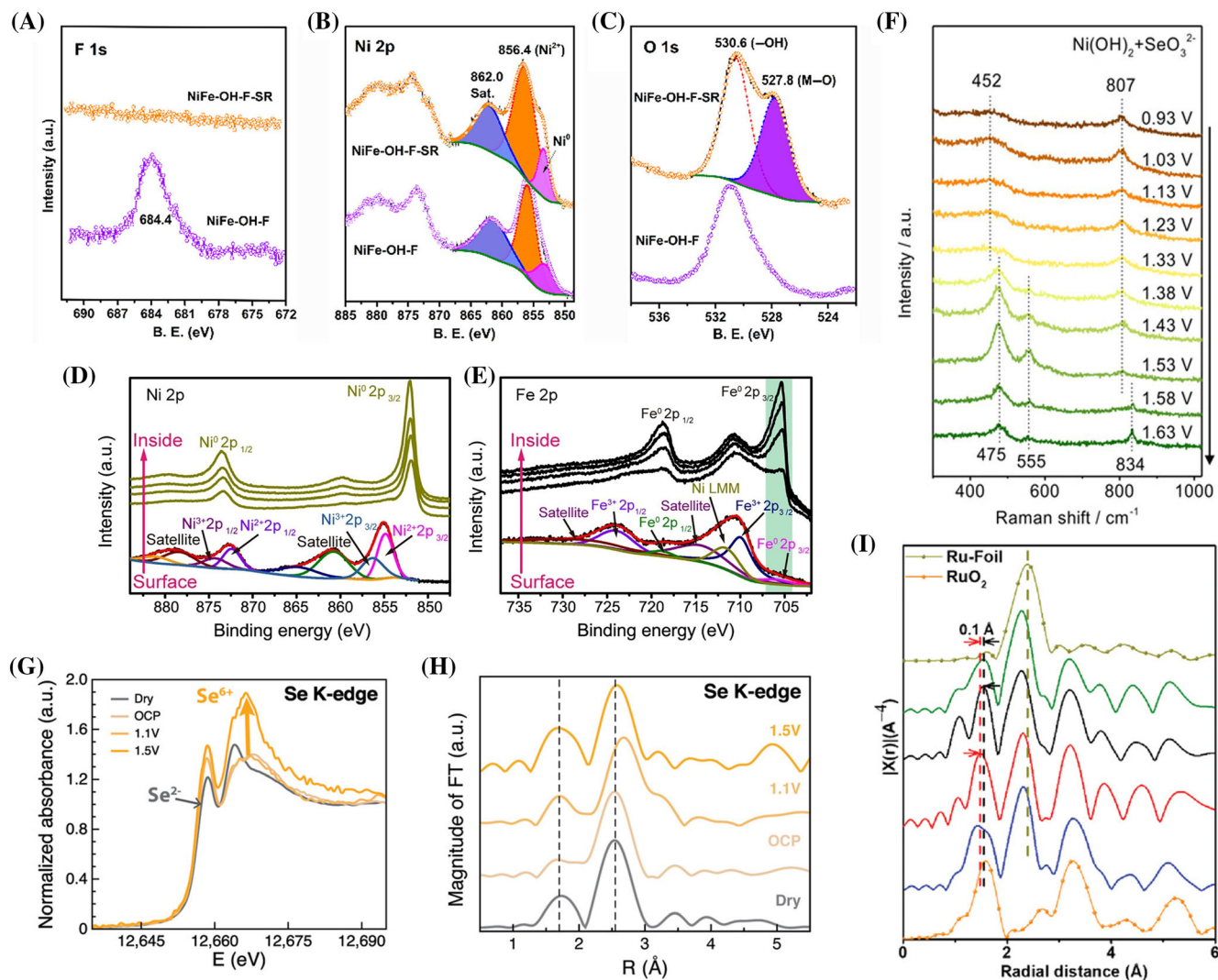


**FIGURE 3** High-resolution XPS spectra of (A) F 1s, (B) Ni 2p, and (C) O 1s. Reproduced with permission.<sup>40</sup> Copyright 2019, American Chemical Society. XPS depth profile of (D) Ni 2p and (E) Fe 2p for  $\text{Fe}_{0.4}\text{Ni}_{0.6}$  alloy fiber paper after OER testing. Reproduced with permission.<sup>42</sup> Copyright 2021, Elsevier Inc. (F) In situ Raman spectra of  $\text{NiSe}_2$  under OER condition. Reproduced with permission.<sup>44</sup> Copyright 2020, Wiley-VCH. In situ (G) XANES K-edge and (H) EXAFS radial distribution function of Se. Reproduced with permission.<sup>46</sup> Copyright 2021, Wiley-VCH. (I) Ru K-edge FT-EXAFS profiles of  $\text{Ni-Ru@RuO}_x$  compared with those of  $\text{Ni-Ru@RuO}_x\text{-EL}$ ,  $\text{Ni-Ru@RuO}_x\text{-CL}$  and  $\text{Ni-Ru@RuO}_x\text{-HL}$ . Reproduced with permission.<sup>47</sup> Copyright 2021, Wiley-VCH.

in situ TEM. Upon applying an oxidation potential, the size of the  $\text{AgNbO}_3$  particle was reduced 20 nm due to the leaching of Nb. By doing so, we successfully demonstrate the removal of surface Ag nanoparticles and expose a fresh structural lattice of  $\text{AgNbO}_3$  perovskite, which benefits the targeted electro-synthesis.<sup>37</sup> Furthermore, atomic force microscopy (AFM) is a highly sensitive equipment that provides detailed information about the surface roughness of a catalyst at the atomic level. Jaramillo documented the development of an  $\text{IrO}_x/\text{SrIrO}_3$  electrocatalyst obtained from thin layers of  $\text{SrIrO}_3$ .<sup>38</sup> The AFM image of the  $\text{SrIrO}_3$  thin film, taken after a 30-h test, reveal a significant alteration in the surface. This change is ascribed to the substantial loss of Sr atoms by leaching.

### 3.2 | Spectroscopic characterizations

Component leaching during OER generally results in variations in the chemical bonds of catalysts, which can be inquired by spectroscopy analysis instruments such as x-ray photoelectron spectroscopy (XPS), Raman spectroscopy, x-ray absorption spectroscopy (XAS), and et al. XPS is a commonly employed technique for evaluating electronic structures, with a specific focus on the surface. It provides detailed information about the outermost 1–10 nanometers of the samples.<sup>39</sup> Hu et al. revealed the surface self-reconstruction of the F-doped nickel-iron hydroxide ( $\text{NiFe-OH-F}$ ) for OER by ex situ XPS.<sup>40</sup> As observed from Figure 3A–C, the F 1s peak disappeared

while new peaks emerged in the O 1s spectra of after the OER tests. This indicates that a substantial quantity of F leached from the catalyst and the surface changed into a F-free NiFe material. XPS is also used to unveil the leaching of Cl ions in perovskite-based material.<sup>41</sup> Very recently, the Qiu group collected the XPS depth profile to investigate the surface of Fe<sub>0.4</sub>Ni<sub>0.6</sub> alloy after OER.<sup>42</sup> Comparing Figure 3D with Figure 3E, the Fe was prioritized to be oxidized and partially leached into the electrolyte, thus exposing more Ni to generate active oxyhydroxide species.

Raman spectroscopy is an effective method for examining the vibrational characteristics of chemical bonds, offering a distinctive structural identifier.<sup>43</sup> The Zhang group utilized in situ Raman spectroscopy to reveal the enhancement of the OER activity.<sup>44</sup> Figure 3F revealed that the stretching of Se—Se bonds in NiSe<sub>2</sub>, decreased in intensity as the potential increased. This indicates that there was a significant loss of Se. A peak with a wavenumber of 834 cm<sup>-1</sup>, corresponding to the (SeO<sub>4</sub><sup>2-</sup>) ion, was observed at an increased potential. Therefore, it is hypothesized that the Se experienced a process of leaching and oxidation, resulting in SeO<sub>4</sub><sup>2-</sup> being the actual form of Se under the OER situation.

XAS can be categorized into two main regions: x-ray absorption near edge structure (XANES) and extended x-ray absorption fine structure (EXAFS), which can reveal the electronic states and the surrounding coordination geometry of the target atoms, respectively.<sup>45</sup> The Sargent group examined the structural changes of the electrode material under OER using in situ XAS measurements.<sup>46</sup> Figure 3G,H shows the XAS spectra of the Se K-edge for the (NiCo)<sub>3</sub>Se<sub>4</sub> catalyst. The average oxidation state of Se increased from -2 to +6 as the anodic potentials were applied. Additionally, there was a gradual enhancement in the intensity of the Se-O peak at a distance of 1.7 Å. This observation provides evidence that Se was being released electrochemically. Chen et al. also noticed a similar effect in their study.<sup>11</sup> In a recent study conducted by the Kim group, they observed a shorter Ru—O bond length in the Ni-Ru@RuOx-EL compared to the RuO<sub>2</sub> reference. This was demonstrated by the Ru K-edge displayed in Figure 3I.<sup>47</sup> The compressed Ru core was linked to the leaching of Ni in the acidic electrolyte.

### 3.3 | Other techniques

There are also other techniques that can help determine the component leaching of the OER catalysts. Among them, inductively coupled plasma is the most widely used technique, which provides element analysis to indirectly certify the leaching of catalyst component. For instance, Jaramillo et al. utilized inductively coupled plasma-mass

spectrometry (ICP-MS) to evaluate the electrolyte and found evidence of Sr and Ir leaching during testing.<sup>48</sup> Figure 4A recorded the Sr and Ir dissolution percentages after OER test on five different electrodes. It has been observed that the leaching rates are faster for materials with higher nominal Sr concentrations. Additionally, all of the synthesized catalysts, except for Sr<sub>4</sub>IrO<sub>6</sub>, exhibit lesser Ir dissolution than the commercial Ir/C catalyst.

Isotopic labeling is a technique employed to monitor the movement of an isotope during a chemical reaction. Markovic et al. studied the activity-stability trend of the Fe-M hydr(oxy)oxides (Fe-MO<sub>x</sub>H<sub>y</sub>) catalysts by isotopic labeling experiments.<sup>49</sup> The Fe isotopes were examined by manufacturing the catalysts using <sup>56</sup>Fe and conducting OER test in an electrolyte containing <sup>57</sup>Fe. Figure 4B reveals the dynamic exchange (leaching and redeposition) of Fe during OER. The rapid dissolution of <sup>56</sup>Fe from the electrode is promptly followed by the instantaneous redeposition of <sup>57</sup>Fe from the electrolyte. This maintains a consistent concentration of Fe at the surface of the electrode, which is evident from the sustained high activity of OER that does not diminish throughout the experiment.

In addition, the electrochemical quartz crystal microbalance (EQCM) is a highly effective method that combines electrochemistry with quartz crystal microbalance to study the surface dynamics of OER catalysts. In 2018, the Grimaud group initially utilized this weight-sensitive approach to investigate the breakdown process of the Ni-based crystalline oxides.<sup>50</sup> Based on the data presented in Figure 4C, it can be inferred that the LaNiO<sub>3-δ</sub> catalyst has negligible mass loss when undergoing OER cycling. An analogous observation was noted for the amorphous Ni(Fe)OOH film. In contrast, La<sub>2</sub>Li<sub>0.5</sub>Ni<sub>0.5</sub>O<sub>4</sub> exhibited noticeable and voltage-dependent reduction in mass above 1.5 V versus RHE.

## 4 | INACTIVE COMPONENT LEACHING DURING OER

In theory, component leaching during electrocatalysis would result in activity degradation. However, in the field of OER, the inactive component leaching would lead to a significantly improved OER performance rather than sacrificing the catalytic activity. The OER catalysts are divided into different groups: spinel family, perovskite oxides and pyrochlores, layered structure family, intermetallic compounds, polyoxometalate (POM)-based materials, and anion-decorated metal compounds. According to the unique structure and electronic properties of each category of materials, the corresponding leaching behavior as well as the induced effect are discussed in detail, and the progress in manipulating

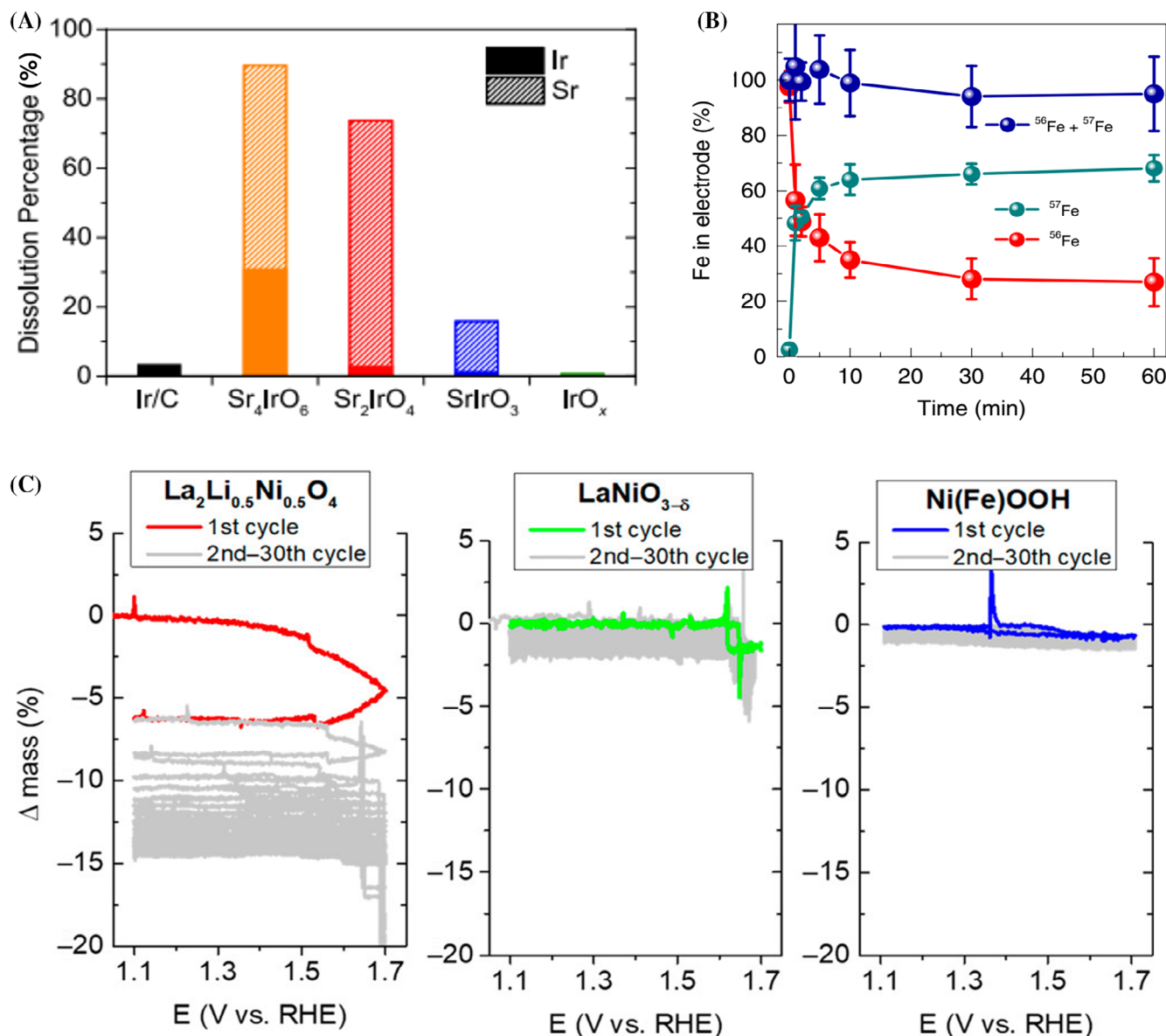


**FIGURE 4** (A) Ir (solid bars) and Sr (striped bars) dissolution percentages after stability testing of initial loaded amount on the electrode for Sr<sub>4</sub>IrO<sub>6</sub>, Sr<sub>2</sub>IrO<sub>4</sub>, SrIrO<sub>3</sub>, IrO<sub>x</sub>, and Ir/C (Premetek) measured by ICP-MS. Reproduced with permission.<sup>48</sup> Copyright 2019, American Chemical Society. (B) The total amount of Fe in the Fe-NiO<sub>x</sub>H<sub>y</sub> electrode obtained by isotopic labeling experiments. Reproduced with permission.<sup>49</sup> Copyright 2020, Nature Publishing Group. (C) Comparison of the mass loss of La<sub>2</sub>Li<sub>0.5</sub>Ni<sub>0.5</sub>O<sub>4</sub>, LaNiO<sub>3-δ</sub>, and Ni(Fe) hydroxide catalysts upon cycling in KOH solution (pH = 13) recorded by EQCM. Reproduced with permission.<sup>50</sup> Copyright 2018, American Chemical Society.

leaching amount/degree toward a tunable surface evolution is summarized. Moreover, special attention is paid to the hot topic that why the in situ formed species after leaching of inactive component are often more active than the originally synthesized ones.

#### 4.1 | Spinel family

Spinel oxides, which have the general formula AB<sub>2</sub>O<sub>4</sub>, are a significant type of anode material for the OER.<sup>51–53</sup>

Over the past years, numerous spinel oxides have been investigated by altering cation A at tetrahedra sites or cation B at octahedral sites, and among them, cobalt oxide (Co<sub>3</sub>O<sub>4</sub>) has received particular interest because of its promising OER activity and stability.<sup>54–56</sup>

The Menezes group determined the specific role of tetrahedral and octahedral sites in the OER. They used two spinel materials, Zn<sup>II</sup>Co<sup>III</sup><sub>2</sub>O<sub>4</sub> and Co<sup>II</sup>Co<sup>III</sup><sub>2</sub>O<sub>4</sub> (Co<sub>3</sub>O<sub>4</sub>) to identify the active sites for the OER.<sup>57</sup> The superior activity of ZnCo<sub>2</sub>O<sub>4</sub> compared to Co<sub>3</sub>O<sub>4</sub> indicates that the presence of Co<sup>II</sup> is not necessary for



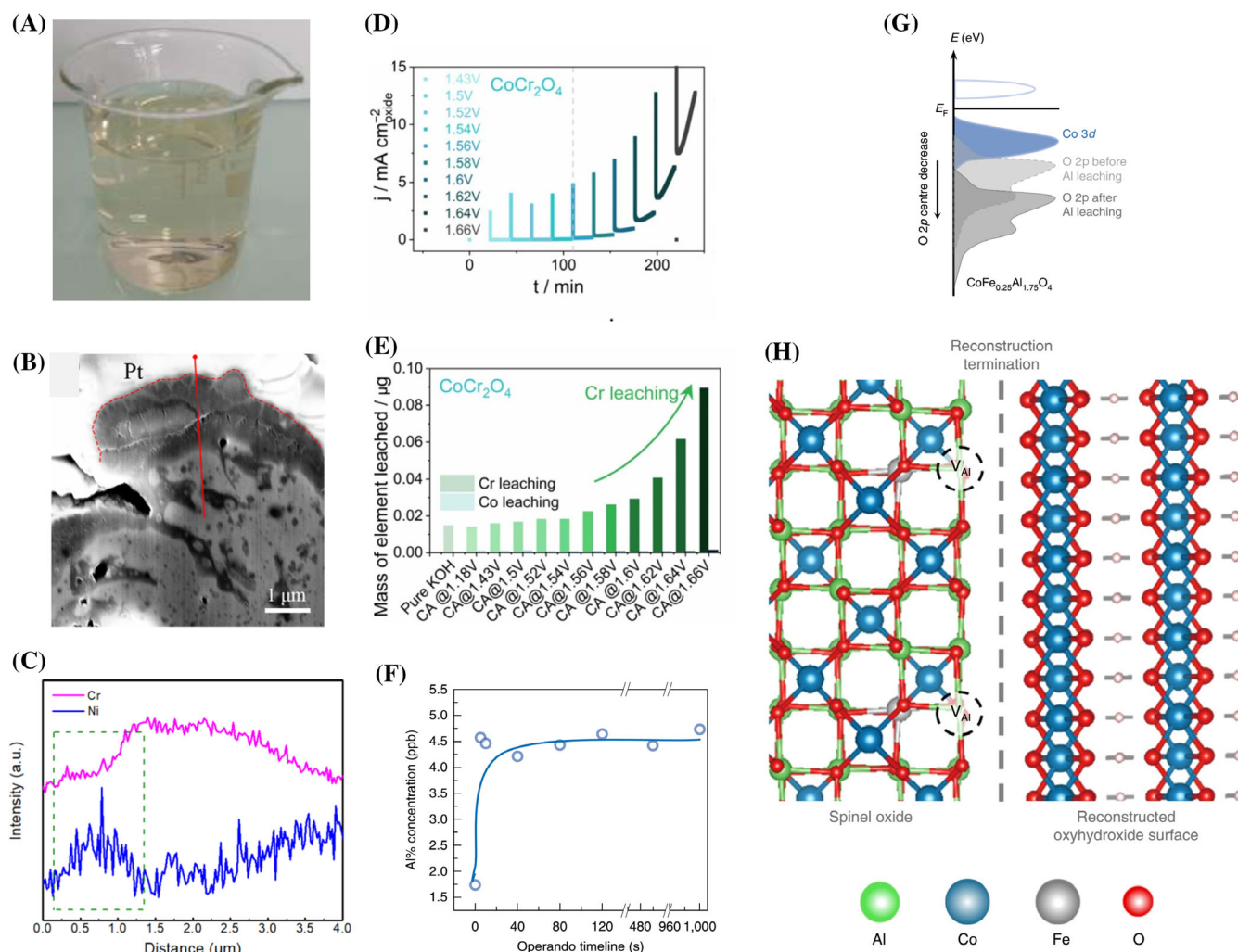


**FIGURE 5** (A) Digital photograph of 1.0 M KOH solution after activation. (B) FIB cross-sectional SEM image of a single microsphere after activation. (C) EDS linear scanning profiles along the red line. Reproduced with permission.<sup>60</sup> Copyright 2020, American Chemical Society. (D) A consecutive series of CA at different potentials from 1.43 to 1.66 V for CoCr<sub>2</sub>O<sub>4</sub>. (E) The cumulative mass of element leached after consecutive series of CA conducted at 20 min interval for CoCr<sub>2</sub>O<sub>4</sub>. Reproduced with permission.<sup>61</sup> Copyright 2021, Wiley-VCH. (F) ICP-MS test of the electrolyte for CoFe<sub>0.25</sub>Al<sub>1.75</sub>O<sub>4</sub> cycling under an operation time of 0–1000 s (in 1 M KOH under 20 μA cm<sup>-2</sup>). (G) Schematic band diagrams of CoFe<sub>0.25</sub>Al<sub>1.75</sub>O<sub>4</sub> with and without Al<sup>3+</sup> vacancies. (H) Schematic of CoFe<sub>0.25</sub>Al<sub>1.75</sub>O<sub>4</sub>, which terminates its surface reconstruction due to the termination of lattice oxygen oxidation. Reproduced with permission.<sup>64</sup> Copyright 2019, Nature Publishing Group.

catalyzing OER. Additionally, it was discovered that the leaching of zinc from the surface resulted in the formation of numerous structural defects. These defects played a crucial role in stabilizing the active Co<sup>IV</sup> intermediate by oxidizing Co<sup>III</sup>. As a result, the rate of OER was accelerated. Notably, in this case, the leaching of Zn doesn't affect the surface morphology of the ZnCo<sub>2</sub>O<sub>4</sub> spinel. In addition to cobalt oxide, iron-based spinel oxides have also been extensively studied as catalysts for the OER because of the abundance in the Earth.<sup>58,59</sup> The Zhong group created a catalyst called Ni/Cr-incorporated Fe<sub>3</sub>O<sub>4</sub>, which showed exceptional performance in the OER.<sup>60</sup> Throughout the OER process, the electrolyte gradually

changed to a light yellow color (Figure 5A). The EDS profiles (Figure 5C) obtained from Figure 5B showed that the surface became enriched with Ni while Cr was absent. The Cr element served as a sacrificial agent, enhancing the exposure of extra active sites.

Xu group further focused on manipulating cation leaching in the spinel catalysts to promote surface reconstruction in a tunable fashion.<sup>61–63</sup> Remarkably, the controlled extraction of Cr in CoCr<sub>2</sub>O<sub>4</sub> was realized with the application of high potentials, resulting in substantial enhancement in OER activity. As revealed from Figure 5D,E, the amount of Cr dissolved is linearly positively related to the applied potential. Moreover, the



occurrence and acceleration of Cr leaching synchronized with the OER activity. Through further characterizations, it was established that the leaching of Cr enables the Co species to undergo a transformation into active Co oxyhydroxides that were different from CoOOH. A different study conducted by the same group presented a method involving iron substitution to enhance the reactivity of  $\text{CoAl}_2\text{O}_4$ .<sup>64</sup> As confirmed in Figure 5F, the Al leaching process completed rapidly, and no further Al dissolution occurs. DFT study illustrated that the O 2p decreased in by introduction of vacancies from Al leaching (Figure 5G). Consequently, the reconstruction was terminated as no more  $\text{V}_\text{O}$  were provided (Figure 5H). These findings will provide new ideas for altering the dynamic reconstruction process in order to optimize the active sites, leading to the development of durable and cost-effective catalysts for the OER. In the work of Xu group, the surface of the spinel changes into an amorphous phase.<sup>60,61</sup> Generally, a thin layer with a thickness of several nanometers would form on the surface of the spinel. The newly formed amorphous phase is the real electrocatalysis center.

For a short summary, inactive elements can be incorporated and subsequently leached in both the A and B sites of the spinel oxides. Inactive element leaching accelerates the OER performance of spinel oxides in the following aspects: (a) creating defects, (b) exposing active sites, and (c) forming unconventional active species. Besides these fundamental aspects, pioneer works also showed the manipulation of inactive cation leaching is an effective way to tune the OER performance.

## 4.2 | Perovskites and pyrochlores

The formula of perovskite oxide is  $\text{ABO}_3$ , with A sites having a coordination number of 12, while the B-sites accommodate cations in corner-sharing  $\text{BO}_6$  octahedra. Perovskite oxides have recently become a focus of research due to their adaptable structure and adjustable OER activity.<sup>65–67</sup> In 2012, the Shao-Horn group first investigated the surface structural stability of the perovskites after water oxidation in the alkaline media.<sup>68</sup> They selected a series of perovskites and studied their surface structural evolution using HRTEM and Raman spectroscopy. Figure 6A displays the HAADF image of five times cycled BSCF, and the quantification of the EDS results plotted against distance from the surface was revealed in the Figure 6B. The remarkable decreases in the amounts of  $\text{Ba}^{2+}$  and  $\text{Sr}^{2+}$ , indicate the leaching of A-site cations during the catalysis. The surface of BSCF82 was demonstrated to undergo quick surface amorphization under OER condition, and the newly generated layer containing

mainly Co and Fe contributes to the enhanced activity while other perovskites with lower OER performance did not undergo such transformation. With the help of the emerging in situ methodology, the Schmidt group has additionally verified that the amorphous  $\text{Fe/Co(O)OH}$  generated on the BSCF surface, which is regarded as the real active species (Figure 6C).<sup>69</sup> Jaramillo et al. discovered Sr leaching from  $\text{SrIrO}_3$  perovskite during the OER test.<sup>38</sup> The in situ generated  $\text{IrO}_x/\text{SrIrO}_3$  catalyst demonstrated superior OER activity of perovskite catalysts in acidic electrolyte for the first time, outperforming the known  $\text{IrO}_x$  and  $\text{RuO}_x$  catalysts that have reasonable acidic OER activities. DFT calculations suggested the possible formation of  $\text{IrO}_3$  or anatase  $\text{IrO}_2$  motifs as highly active surface layer after the Sr leaching.

In general, the A-site leaching would promote the remaining B-site transition metal ions to form surface oxyhydroxide layer. While the A-site itself does not actively engage in OER, the management of the A-site can alter the electrical structure of  $\text{BO}_6$ , hence promoting surface reconstruction to improve the activity of OER. Zhang et al. performed A-site Ce doping in  $\text{LaNiO}_3$  catalyst to regulate the surface reconstruction.<sup>70</sup> The experiment showed that the incorporation of Ce in the A-site greatly reduced the formation potential for the  $\text{NiOOH}$  species, resulting in a 32-fold increase in activity compared to the original  $\text{LaNiO}_3$  electrode. Theoretical calculations further demonstrated that the substitution of Ce causes an upward shift in the center of the O 2p band. This leads to the activation of Ni and promotes the reconstruction of the active phase.

The leaching at the B-site is generally regarded as harmful to the majority of perovskite oxide catalysts. However, there are counter examples in which the performance even becomes better after B-site leaching. The Cherevko group studied the dissolution process of a series of Ir-based oxides in acidic OER.<sup>71</sup> The case study on double perovskite ( $\text{Ba}_2\text{PrIrO}_6$ ) showed that both the non-noble A-site Ba and B-site Pr leached as expected from the thermodynamic data. The leaching of B-site Pr will leave isolated  $\text{IrO}_6$ , and the structure would reconstruct into amorphous (Figure 6D). EDS analysis confirmed the total elimination of Ba and Pr, and the resulting amorphous iridium oxide demonstrated exceptional OER activity. Another work conducted by the Grimaud group introduced a  $\text{La}_2\text{Li}_{0.5}\text{Ni}_{0.5}\text{O}_{4\pm\delta}$  perovskite as OER catalyst.<sup>50</sup> Although the B-site Li experienced continuous leaching, the obtained OER performance even improved. It was discovered that the empty spaces created by Li leaching can increase the activity of OER.

Considering that both A and B site metal cations can be dissolved, Xu et al. conducted a study to understand the leaching effect of A and B on OER activity.<sup>72</sup> By

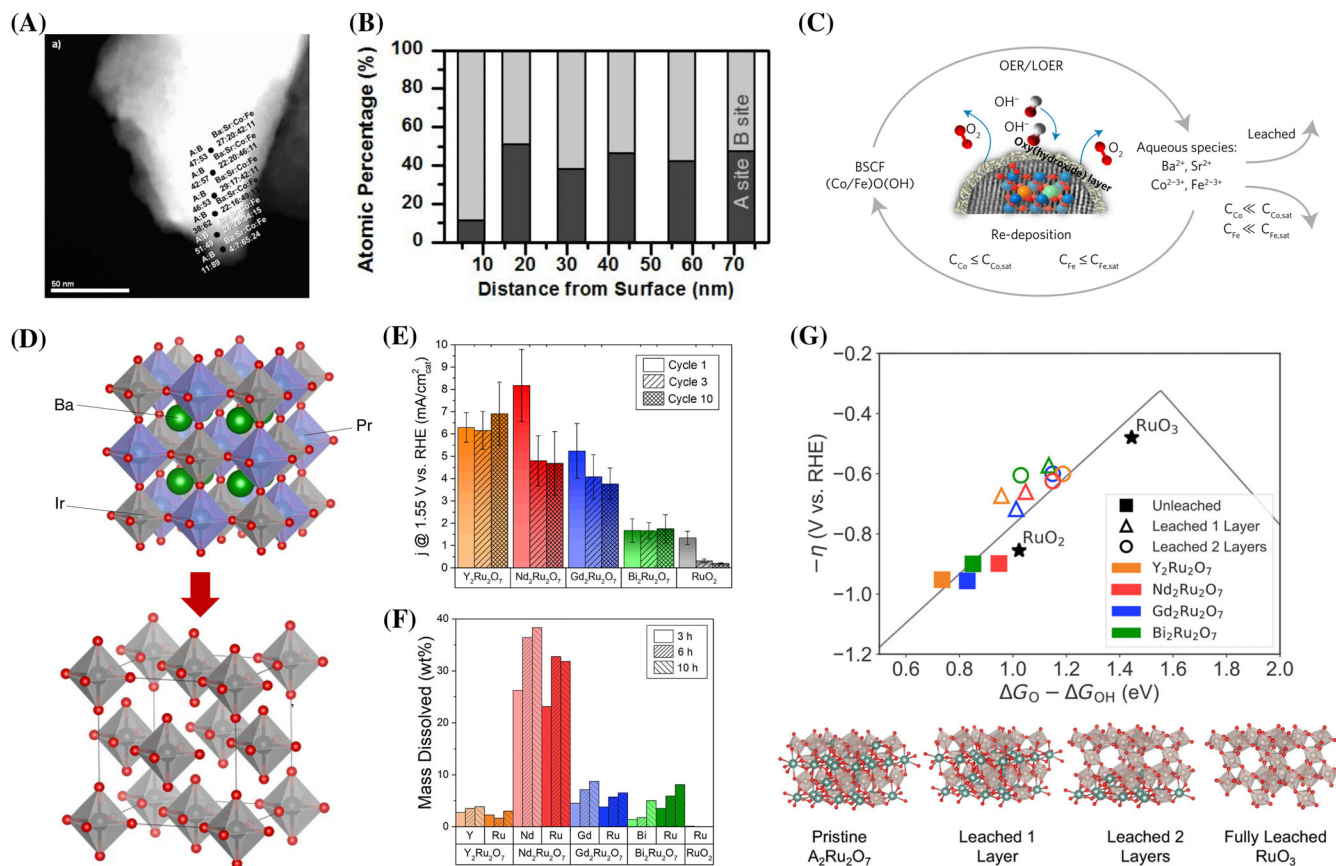


**FIGURE 6** (A) High angular annular dark field (HAADF) imaging and scanning TEM energy dispersive spectroscopy (STEM EDS) of 5 times cycled  $\text{Ba}_{0.5}\text{Sr}_{0.5}\text{Co}_{0.8}\text{Fe}_{0.2}\text{O}_{3-\delta}$  (BSCF82). (B) Quantification of the EDS results showing (A,B) on the HAADF images plotted against distance from the surface. Reproduced with permission.<sup>68</sup> Copyright 2012, American Chemical Society. (C) OER/LOER and dissolution/re-deposition mechanism leading to the formation of a self-assembled active surface layer, rich in  $\text{CoO}(\text{OH})$  and  $\text{FeO}(\text{OH})$ . Reproduced with permission.<sup>69</sup> Copyright 2017, Nature Publishing Group. (D) A leached double perovskite ( $\text{Ba}_2\text{PrIrO}_6$ ) showing isolated  $\text{IrO}_6$  octahedra, which will collapse into an amorphous structure. Reproduced with permission.<sup>71</sup> Copyright 2018, Nature Publishing Group. (E) Average specific activity after 1, 3 and 10 CVs at 1.55 V versus RHE. Error bars represent standard deviation from the average determined from at least three independent measurements. (F) Mass fraction of total deposited catalyst (A-site and Ru) that dissolved in the electrolyte after 3, 6, and 10 h. (G) Activity volcano for pristine and leached pyrochlore phases showing an increase in activity with A-site cation leaching. The structures below show the atomistic models of A-leached surfaces. Reproduced with permission.<sup>73</sup> Copyright 2020, American Chemical Society.

tuning the B-site composition, the surface reconstructions in the model  $\text{SrSc}_{0.5}\text{Ir}_{0.5}\text{O}_3$  (SSI) and  $\text{SrCo}_{0.5}\text{Ir}_{0.5}\text{O}_3$  (SCI) were successfully controlled. The construction procedure was bifurcated into two steps. Initially, the leaching of A-site cations increases the amount of electrochemical area that is accessible for the OER. The second phenomenon involves the development of a reactive  $\text{IrO}_x\text{H}_y$  phase in surfaces, resulting from the leaching of both A and B sites.

Pyrochlore ( $\text{A}_2\text{B}_2\text{O}_7$ , A = nonprecious metal, B = Ir or Ru) complex oxides have shown enhanced OER performance beyond pure Ir/Ru oxides in harsh acidic OER.<sup>73–75</sup> Combining experimental techniques and theoretical calculations, the Jaramillo group investigated how the A site metal affects the OER performance of various Ru-based pyrochlores in acid.<sup>73</sup> Figure 6E,F demonstrates

the correlation between the activity of the OER of the four catalysts and the A-site cations. In addition, they used DFT calculations to theoretically forecast the behavior of OER activity caused by A-site leaching. Figure 6G demonstrates that the activity volcano clearly indicates a noticeable increase in OER activity for reconstructed materials compared to the original pyrochlores. The newly-formed pyrochlore-like  $\text{RuO}_3$  material displays the lowest theoretical overpotential. A similar result was observed from the study of the Schmidt group.<sup>74</sup> They developed several pyrochlores with a lower amount of Ir than commercial  $\text{IrO}_2$ , and the  $\text{Y}_2\text{Ir}_2\text{O}_7$  was demonstrated the most efficient catalyst under OER condition. The enhancement of OER activity of the  $\text{Y}_2\text{Ir}_2\text{O}_7$  catalyst during the stability test was attributed to the leaching of  $\text{Y}^{3+}$ .

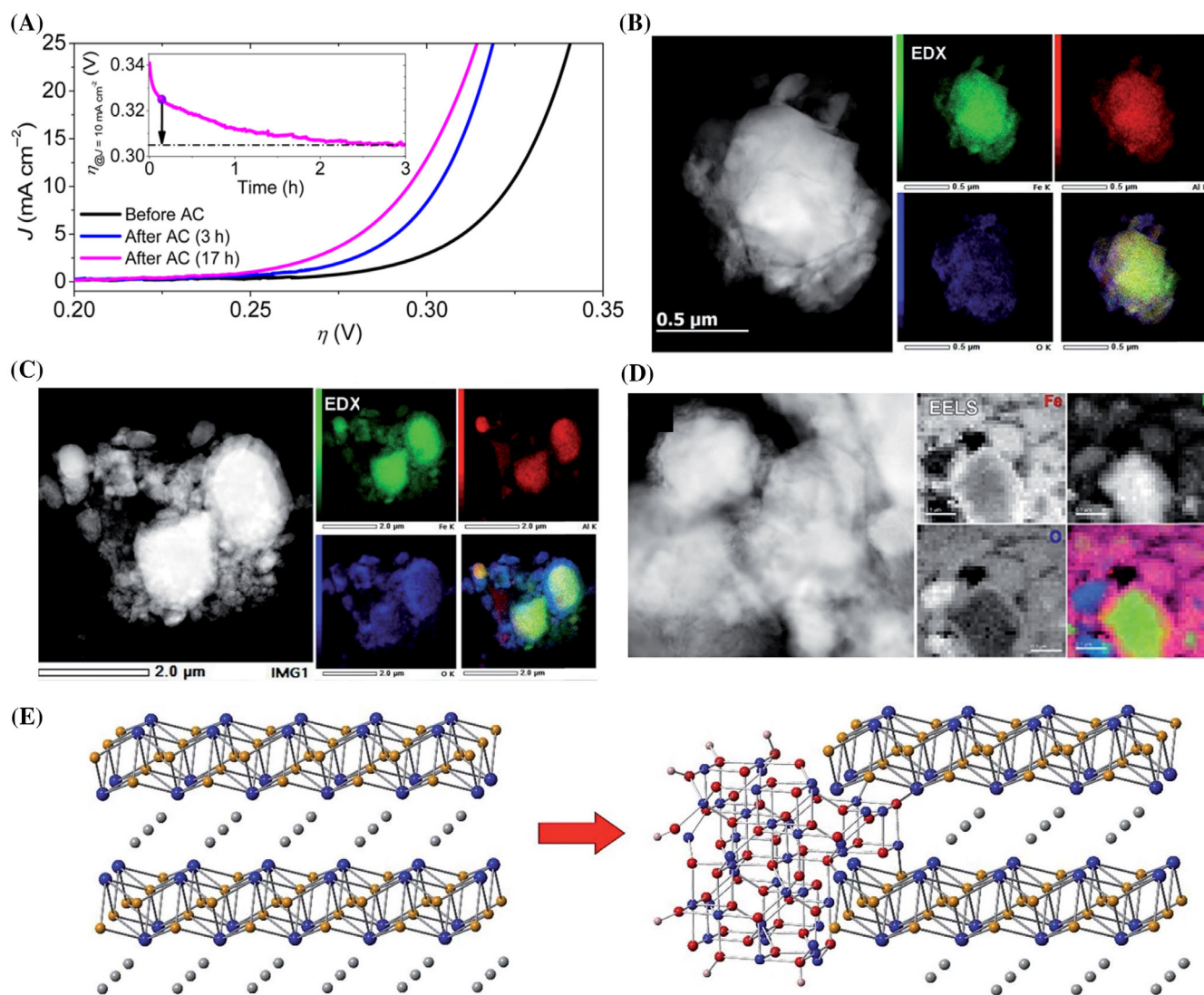


**FIGURE 7** (A) LSV curves showing the effect of continuous anodic conditioning (AC) at  $J = 10 \text{ mA cm}^{-2}$  for CoMn LDH. Reproduced with permission.<sup>77</sup> Copyright 2014, American Chemical Society. HAADF-STEM images and the corresponding STEM-EDX elemental maps of  $\text{AlFe}_2\text{B}_2$  particles (B) before and (C) after electrocatalytic activation in a 1 M KOH solution, where the element distribution is shown with green (Fe), red (Al), and blue (O) colors. (D) EELS mapping of the electrocatalytically activated sample. In the grayscale panels, lighter areas indicate a higher content of the corresponding element. The colored overlay shows the EELS signals for the B-K (green), Fe-L<sub>2,3</sub> (red), and O-K (blue) edges. (E) Hypothesized structure of the electrocatalyst formed from the  $\text{AlFe}_2\text{B}_2$  scaffold. Reproduced under a Creative Commons Attribution-Non Commercial 3.0 Unported License.<sup>79</sup> Copyright 2019, the Authors. Published by Royal Society of Chemistry.

Owing to the more flexible structure of perovskite, the study of inactive cation leaching in perovskite (and analogues) is more abundant than that in spinel. Generally, the A-site cations in the perovskite are easier to leach out. It may be for this reason that the research boom in surface reconstruction began with the study of the leaching of Ba and Sr in BSCF. The inactive B-site cations would undergo a sequential leaching after the A-site cation leaching. This would enhance the degree of surface reconstruction. The widely studied in situ leaching in perovskite has inspired some researchers to disassemble and reassemble perovskites by cation

leaching. This is demonstrated as an efficient approach to the design of superior electrocatalysts.

### 4.3 | Layered structure family

Layered structure catalysts have gained significant interest for OER owing to their distinct advantages such as high surface-to-bulk ratio, controllable structure adjustment and strong structural stability.<sup>76</sup> In 2014, the Hu group developed a Co-Mn layered double hydroxide (LDH) as an OER catalyst.<sup>77</sup> An interesting discovery was



found that the OER performance of this catalyst underwent a significant improvement by anodic conditioning (Figure 7A). ICP-AES investigation revealed that Mn dissolved during OER, resulting in the formation of an amorphous area with a high concentration of undercoordinated Co ions. This could potentially contribute to the increased activity. Another work from the Kundu group obtained a similar conclusion, wherein the activity enhancement induced by dissolving of Sn elements from the layered  $\text{SnCo}(\text{OH})_2$  catalyst was observed.<sup>78</sup> DFT calculations were further performed to help understand the leaching behavior of Sn in OER condition. The study revealed that  $\text{OH}^*$  adsorption on Sn sites exhibited a higher energy preference than that on cobalt sites. Consequently, Sn leaching facilitates the formation of a reactive  $\text{CoOOH}$  compound. This result provided theoretical support for studying leaching phenomenon of the layer structured catalysts when catalyzing OER. Besides, Shatruck et al. developed a layer structured  $\text{AlFe}_2\text{B}_2$  catalyst displaying outstanding OER activity in an alkaline electrolyte.<sup>79</sup> Electron microscopy conducted on the initial and electrochemically activated materials (Figure 7B,C) suggested that aluminum was partially removed from the  $\text{AlFe}_2\text{B}_2$  material during the OER. Moreover, electron energy loss spectroscopy (EELS) was utilized to explore the electronic structures on Fe and B sites. As shown in Figure 7D, after electrochemical activation, the B was regularly found in the reconstructed material, and the  $\text{AlFe}_2\text{B}_2$  nanoparticles featured with an outer layer of  $\text{FeOOH}$ . Based on these analysis, they proposed a catalytic mechanism (Figure 7E) involving partial leaching of Al and the formation of iron oxide during the OER. Similarly, Geng et al. acquired a Fe-Co-Al hydroxide material with a high concentration of defects to achieve exceptional OER activity.<sup>80</sup>

Efforts have been focused on altering the evolution of the surface structure by controlling the loss of cations. An illustrative instance from Lim's research team showcased the use of cation redox to manipulate the leaching voltage of layered  $\text{LiCoO}_{2-x}\text{Cl}_x$ .<sup>81</sup> By utilizing DFT energetics, they studied how the Cl doping altered the structural transformation path. It was found that the Li leaching is energetically unfavorable for the pristine  $\text{LiCoO}_2$ , while for the Cl-contained  $\text{LiCoO}_2$ , all the reaction paths became thermodynamically favorable. Also, the calculated surface formation energy evidenced that the introduction of Cl yielded a favorable creation of oxyhydroxide species, leading to a more satisfactory OER activity.

Layered structure materials feature with a distinct property, that is, a high ratio of basal plane sites to edge sites. Previous works have revealed that the edge sites are

more active than the basal plane sites in the OER. Considering the above, targeted ion leaching at the basal sites to create basal defects can make full use of the abundant basal sites. This may be an interesting research direction for activating layered materials in the near future.

#### 4.4 | Intermetallic compounds

Elemental leaching in intermetallic compounds have emerged as an innovative strategy to boost OER activity.<sup>82,83</sup> As an illustration, Huang et al. investigated the changes in the structure of  $\text{IrNi}_x$  intermetallic compound during the process of OER.<sup>84</sup> It was discovered that a surface Ir-rich skin will be formed owing to the preference leaching of Ni in an acidic environment, while a surface layer that is rich in Ni was seen because of the migration of Ni in an alkaline electrolyte. Moreover, the evolution of catalyst structure both brought self-optimized OER activity. An analogous occurrence was discovered in another study conducted by the Oh group.<sup>85</sup> They applied *operando* XAS and identical location TEM techniques to dynamically monitor the reconstruction process of IrNi catalysts under different pH conditions. As displayed in Figure 8A–I, the IrNi alloy exhibits a surface structure enriched with Ir when electrochemically activated in an acidic electrolyte, while it displays a surface structure enriched with Ni when electrochemically activated in an alkaline electrolyte. Meanwhile, the IrNi (performed in a neutral electrolyte) exhibited a thinner, oxidized Ir oxide shell structure. These results suggest that the property of the intermetallic compound would vary after electrochemical activation and the catalyst structure suitable for certain reactions could be adjusted through the pH condition and applied electric potential.

Generally, the electrochemically oxidized catalysts outperform their thermally treated counterparts. To obtain a deep understanding of this phenomenon, the Friedrich group created an Ir-based catalyst by removing Ru from Ir-Ru alloy using electrochemical leaching.<sup>86</sup> The electrochemical activated catalyst exhibited a 133-fold increase in OER activity compared to the thermally treated counterpart with an equivalent Ir/Ru ratio. EDS analysis coupled with TEM detected only drop of Ru in the electrochemical activated catalyst after 18 h under an anodic potential of 1.6 V, while the thermally treated counterpart showed an unchanged Ir/Ru ratio. The corresponding XPS depth profile in Figure 8J,K agreed well with this outcome. Therefore, it was determined that during the OER, the Ru in the electrochemical activated catalyst underwent a transformation into an unstable Ru hydroxide, which had a tendency to leach into the electrolyte. This was in contrast to the counterpart, where Ru



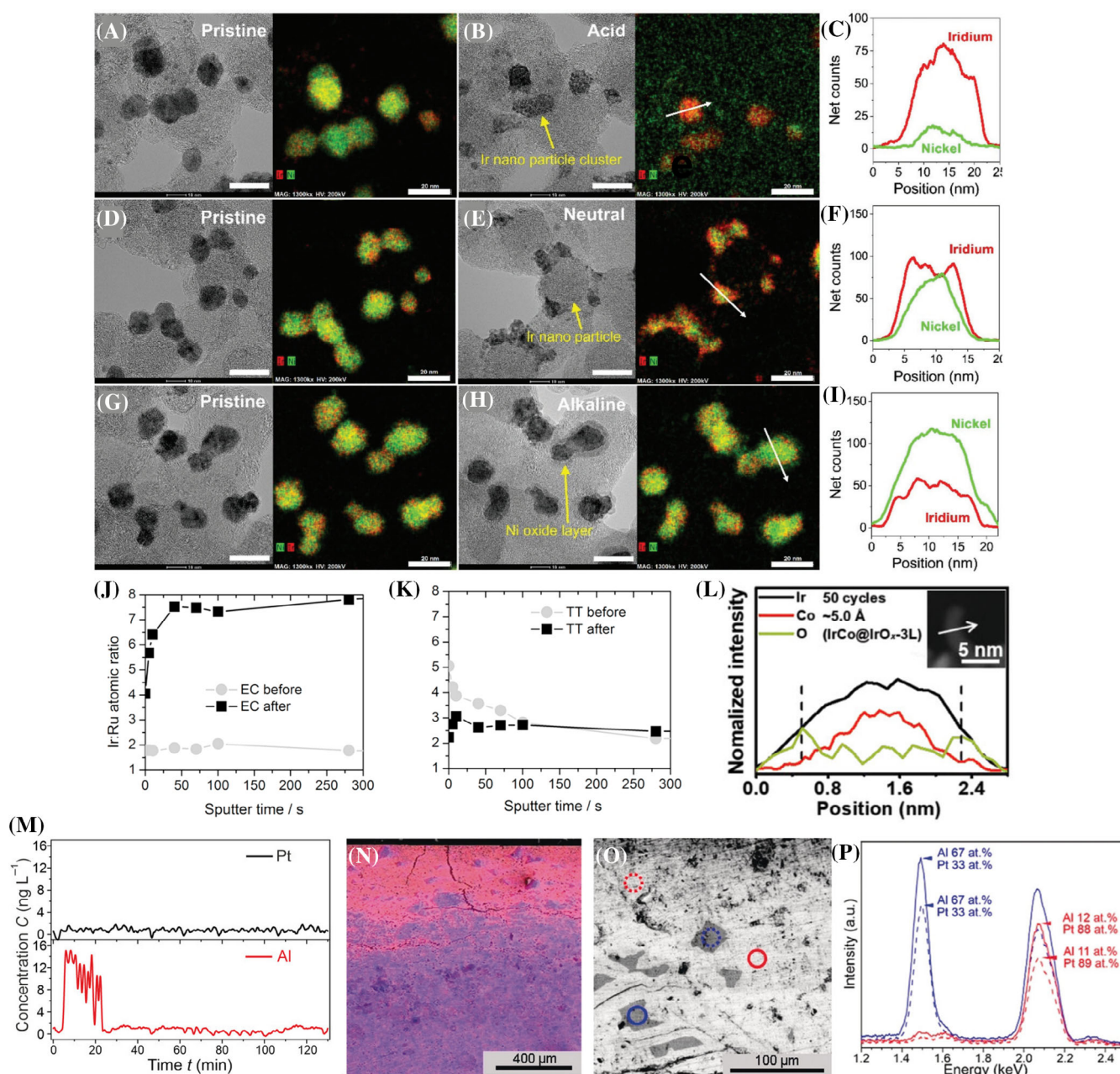


**FIGURE 8** Identical location transmission electron microscopy (IL-TEM) images and IL-HAADF-STEM elemental mapping analysis of pristine IrNi/C before electrochemical activation under (A) acid (d) neutral and (g) alkaline conditions (scale bar: 20 nm). IL-TEM images and IL-HAADF-STEM elemental mapping analysis of electrochemically activated IrNi/C under (B) acid (E) neutral and (H) alkaline conditions, which are denoted as IrNiO<sub>x</sub>/C-A, IrNiO<sub>x</sub>/C-N, and IrNiO<sub>x</sub>/C-Al, respectively (scale bar: 20 nm). Line-scan profiles of (C) IrNiO<sub>x</sub>/C-A, (F) IrNiO<sub>x</sub>/C-N, and (I) IrNiO<sub>x</sub>/C-Al. Reproduced with permission.<sup>85</sup> Copyright 2020, Royal Society of Chemistry. Ex situ XPS analysis of Ir<sub>0.7</sub>Ru<sub>0.3</sub>O<sub>x</sub> (EC) and Ir<sub>0.7</sub>Ru<sub>0.3</sub>O<sub>2</sub> (TT) anodes before and after electrolysis operation for 18 h at 1.6 V: Ir/Ru atomic ratio versus sputter time of the sample (J) EC and (K) TT. Reproduced with permission.<sup>86</sup> Copyright 2017, Elsevier Inc. (L) STEM-EDX line profiles of IrCo@IrO<sub>x</sub>-3L NDs, and the white arrow (insets) indicates the EDX line profile direction. Reproduced with permission.<sup>88</sup> Copyright 2021, Wiley-VCH. (M) Element analysis of effluent electrolyte after chronopotentiometry for 2 h at 10 mA cm<sup>-2</sup>. (N) EDX spectrum image of the top 1.2 mm of the sample (cross section view; Al-rich domains in blue, Pt-enriched grains in red). (O) Back-scattered electron (BSE) image with areas corresponding to the energy-dispersive x-ray spectra (EDX) shown in (P). Reproduced under a Creative Commons CC-BY License.<sup>89</sup> Copyright 2020, the Authors. Published by Wiley-VCH.

was stabilized by Ir in the RuO<sub>x</sub>. The increased activity of the OER in the electrochemically activated catalyst is mostly attributed to the generation of surface O<sup>1-</sup> species

and surface hydroxyl groups. Notably, lattice strain at the interface also has considerable influences on the catalytic activity through altering the local structures of the

interested sites.<sup>87</sup> The Li group selected an IrCo nano-dendrites as a base to electrochemically cultivate IrO<sub>x</sub> and induce interface strain.<sup>88</sup> Following electrochemical treatment in a solution of 0.05 M H<sub>2</sub>SO<sub>4</sub>, the Co was released from the surface, while the Ir underwent a transformation, resulting in the formation of IrO<sub>x</sub> on the surface, as evidenced from Figure 8L. After electrochemical evaluation, the IrCo@IrO<sub>x</sub>-3L catalyst with 1.51% strain exhibited the best activity. DFT calculations further demonstrated that precisely tuned compressive strain facilitated the RDS of OER.

Pt exhibits the highest stability than other noble metals when subjected to OER potentials. Grin et al. reported on the unexpected activity of a surface nanocomposite structure that emerged by the self-organized conversion of the Al<sub>2</sub>Pt intermetallic precursor during the OER.<sup>89</sup> The OER activity improved significantly after a 2 h activation owing to the removing of a surface passive layer of Al. There was no detectable Pt dissolution (Figure 8M). However, a minor quantity of dissolved aluminum was noticed during the initial minutes of the stress test for Al<sub>2</sub>Pt. Characterizations of the cross section were further obtained to get insight into the morphological transformation of the catalyst. As uncovered by Figure 8N–P, the extend of aluminum leaching is around 400 μm, and the abundant fissures facilitate the entry of electrolyte into the bulk material, acting as pathways for Al leaching. Following these findings, the Antonyshyn group further studied a series of isostructural compounds M<sub>2</sub>Pt (M = Al, Ga, In, Sn) as OER catalysts.<sup>90</sup> Their activity followed the trend In<sub>2</sub>Pt > Ga<sub>2</sub>Pt > Al<sub>2</sub>Pt > Sn<sub>2</sub>Pt, depending on the property of M and its leaching rate under OER condition. The enhanced OER activity can be ascribed to the substantial quantity of Pt present on the surface, as well as the altered electronic state of Pt resulting from the introduction of metal M.

Intermetallic compounds composed of non-precious metals and precious metals are the most common objects for the study of ion leaching. In most cases, the non-precious metals preferentially dissolve, leading to a surface enriched with more active and stable precious metal oxide/hydroxide in an amorphous phase. This process can significantly alter the surface composition, structure, and catalytic properties of the intermetallic compound. Future work could focus on rational design of intermetallic compounds with controlled leaching behavior to balance activity and stability for the OER.

## 4.5 | POM-based materials

POMs are a diverse group of metal oxyanions that consist of a wide variety of crystalline inorganic clusters. These clusters possess an unparalleled array of physical and

chemical properties. POM-based materials, which have adjustable compositions and a wide range of morphologies, are being recognized as electrocatalysts for OER because of their rich redox chemistry.<sup>91</sup>

Mai group presented a novel polyoxomolybdate-organic complex that exhibits a stable coordination between the metal center (Ni<sup>2+</sup> and [Mo<sub>8</sub>O<sub>26</sub>]<sup>4−</sup>) and the organic ligand.<sup>92</sup> Following the introduction of Fe, a set of Fe-doped Ni-POMo materials having porous and amorphous architectures were created. The presence of these characteristics expedited the diffusion-leaching mechanisms of both ligands and anions, leading to swift and thorough phase reconstruction during OER. As revealed from the Mo, N, and Ni XPS spectra of Fe<sub>0.052</sub>Ni-POMo catalyst under (Figure 9A–C), the absence of Mo and N peaks indicated that the ligand and anion were leached together. In contrast, the Ni and Fe peaks rose to higher values after activation and remained stable during the 500-h test, indicating the creation of high-valence Ni/Fe species and the robust stability of the catalyst. An analogous outcome was noted in a study conducted by the Selomulya group.<sup>93</sup> In another study, Zhao et al. observed distinct reconstruction behaviors of the hydrate/anhydrous molybdate pre-catalyst.<sup>94</sup> For the hydrate NiMoO<sub>4</sub>·xH<sub>2</sub>O, a complete reconstruction was observed, resulting in the formation of an ultrasmall nanoparticle-interconnected multilevel structure. The presence of a loose reconstruction layer, resulting from the simultaneous leaching of crystal water and MoO<sub>4</sub><sup>2−</sup>, plays a crucial role in facilitating the thorough penetration of the solution and, consequently, enabling complete reconstruction (as shown in Figure 9D–I). For anhydrous NiMoO<sub>4</sub>, alkali etching does not completely dissolve the crystal structure. A thick layer is created which hinders the penetration of electrolyte for further etching or reconstruction.

POMs represent an interesting and versatile class of compounds for OER, offering tunable structures, redox activity, and stability. The incorporation of organic moieties, heteroatoms, and waters of hydration within the POM structure influences both the leaching dynamics and the efficacy of the OER process.

## 4.6 | Anion-decorated metal compounds

Since the early report of highly active MoS<sub>2</sub> for hydrogen evolution reaction, anion-decorated metal compounds (M-X, X from group IIIA to VIA) including metal chalcogenides, pnictides, borides, chlorides, fluorides, phosphates, sulfate, carbonate, and so on have represented another material family of efficient OER catalysts.<sup>95–99</sup> However, a number of groups have found the fast



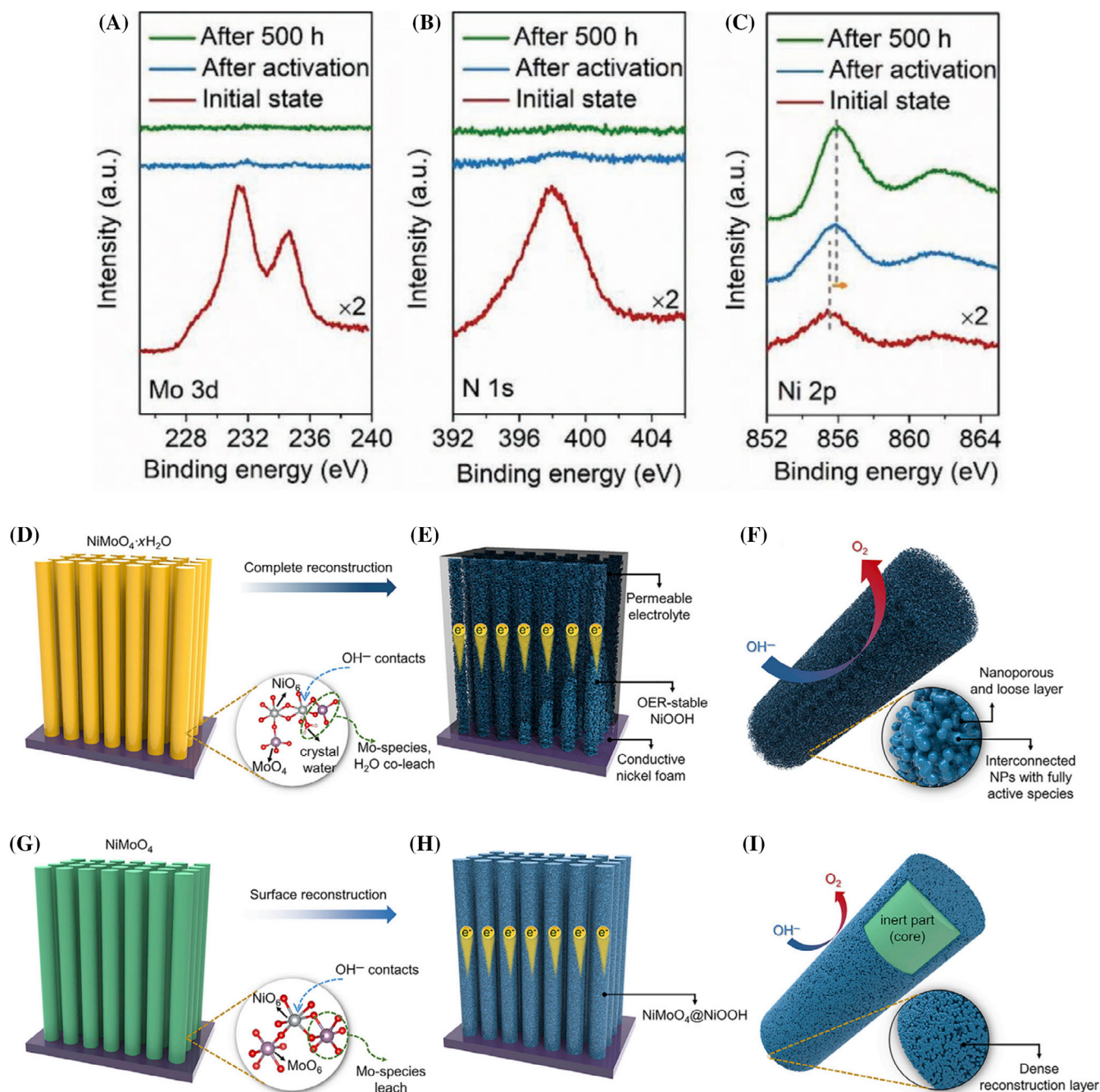


**FIGURE 9** (A) Mo 3d, (B) N 1s and (C) Ni 2p XPS spectra of  $\text{Fe}_{0.052}\text{Ni-POMo}$  initially, after CV activation and after OER for 500 h. Reproduced with permission.<sup>92</sup> Copyright 2021, Wiley-VCH. (D–F) Etching-leaching-reconstruction engineering to achieve complete reconstruction of  $\text{NiMoO}_4 \cdot x\text{H}_2\text{O}$  (g–i) Surface reconstruction of  $\text{NiMoO}_4$  to form core-shell  $\text{NiMoO}_4 @ \text{NiOOH}$ , with the low reconstruction degree limited by a dense reconstruction layer. Reproduced with permission.<sup>94</sup> Copyright 2020, Elsevier Inc.

leaching of anions and phase transition of these catalysts under OER condition, so they call these anion-decorated metal compounds “pre-catalysts”.<sup>11,18,19</sup> For example, the Hu group showed that the F element in  $\text{NiFe-OH-F}$  undergoes removal, leading to accelerated surface rebuilding (Figure 3A), and the OER activity increased over 58-fold after the reconstruction process.<sup>40</sup> Another work from the Driess group obtained a similar

conclusion.<sup>100</sup> The FeAs that was deposited experienced corrosion in a highly alkaline anodic environment. This led to significant leaching of As in the electrolyte, resulting in the formation of an active ferrihydrite phase. Crucially, the As that is dissolved in the electrolyte can be completely electrodeposited at the counter electrode, resulting in an environmentally friendly procedure. Furthermore, Song et al. introduced a new OER pre-catalyst

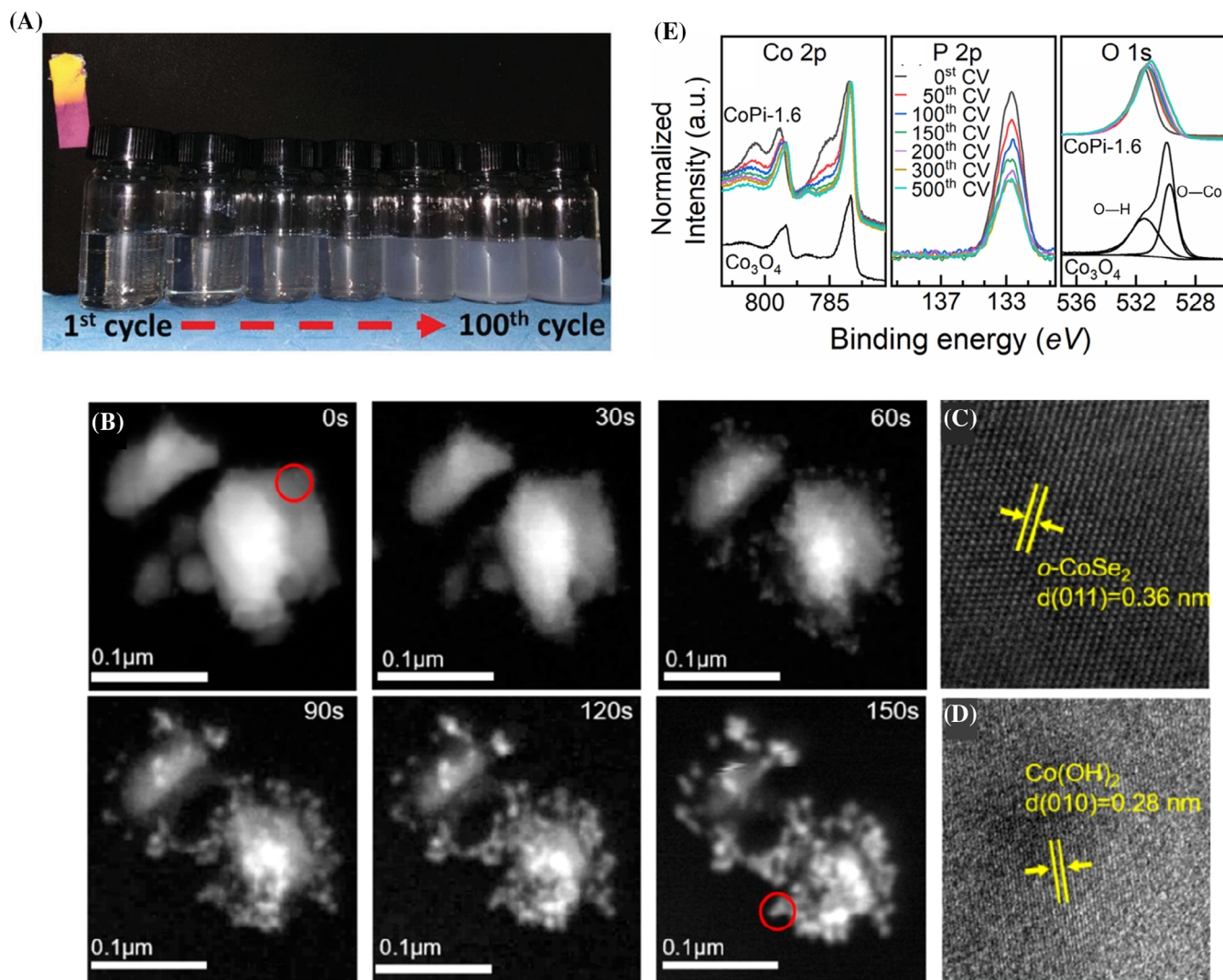


**FIGURE 10** (A) Optical photos for the detection of  $\text{Cl}^-$  in electrolyte with increasing CV cycles. Reproduced with permission.<sup>101</sup> Copyright 2019, Wiley-VCH. (B) In situ STEM images of the  $\text{CoSe}_{1.26}\text{P}_{1.42}$  catalyst taken at different time after immersing in the KOH solution. HRTEM images of the selected region of the (C) initial and (D) final states of the  $\text{CoSe}_{1.26}\text{P}_{1.42}$ . Reproduced with permission.<sup>11</sup> Copyright 2019, American Chemical Society. (E) Evolution of the Co 2p, P 2p, and O 1s XPS spectra of CoPi-1.6 as a function of the number of CV sweeps. Reproduced under a CC-BY-NC-ND 4.0 License.<sup>102</sup> Copyright © 2021, the Authors. Published by American Chemical Society.

cobalt oxychloride ( $\text{Co}_2(\text{OH})_3\text{Cl}$ ) showing outstanding performance toward OER.<sup>101</sup> To verify the anion leaching during the electrochemical activation,  $\text{AgNO}_3$  aqueous solution was used to detect  $\text{Cl}^-$  ions in the electrolyte. As displayed in Figure 10A, clearly, with increasing number of CV cycles, more AgCl precipitates, demonstrating the continuous leaching of the lattice  $\text{Cl}^-$  during the activation. *Operando* XAS characterization together with DFT calculations disclosed that the leaching of lattice  $\text{Cl}^-$  played key roles in triggering the structural evolution, and the increased OER performance rooted in the coordination-unsaturated sites induced by  $\text{Cl}^-$  leaching. Extensive research has been carried out to gain insights into the morphological and chemical changes the anions undergo during the activation process. Figure 10B–D illustrates the in situ TEM images

which revealed the leaching of Se in  $\text{CoSe}_2$ .<sup>11</sup> Eventually, the  $\text{CoSe}_2$  was transformed into  $\text{Co}(\text{OH})_2$ . In a work from the Creatore group, changes in CoPi upon activation were unveiled by XPS measurements.<sup>102</sup> Figure 10E displays the changes in the Co 2p and P 2p XPS spectra of CoPi-1.6 as the number of CV sweeps varies. The change from  $\text{Co}^{2+}$  to  $\text{Co}^{3+}$  occurred as the number of CV cycles increased. Concurrently with the alteration in Co, the comparative magnitude of the P 2p spectra diminished, suggesting the removal of phosphate species. Moreover, using potential-dependent *operando* Raman spectroscopy, the Zhang group demonstrated the evolution of chalcogenates under OER potentials (Figure 3F).<sup>44</sup> As the potential increased, the Se in  $\text{NiSe}_2$  underwent oxidation. In OER circumstances, selenate is the actual form of Se.



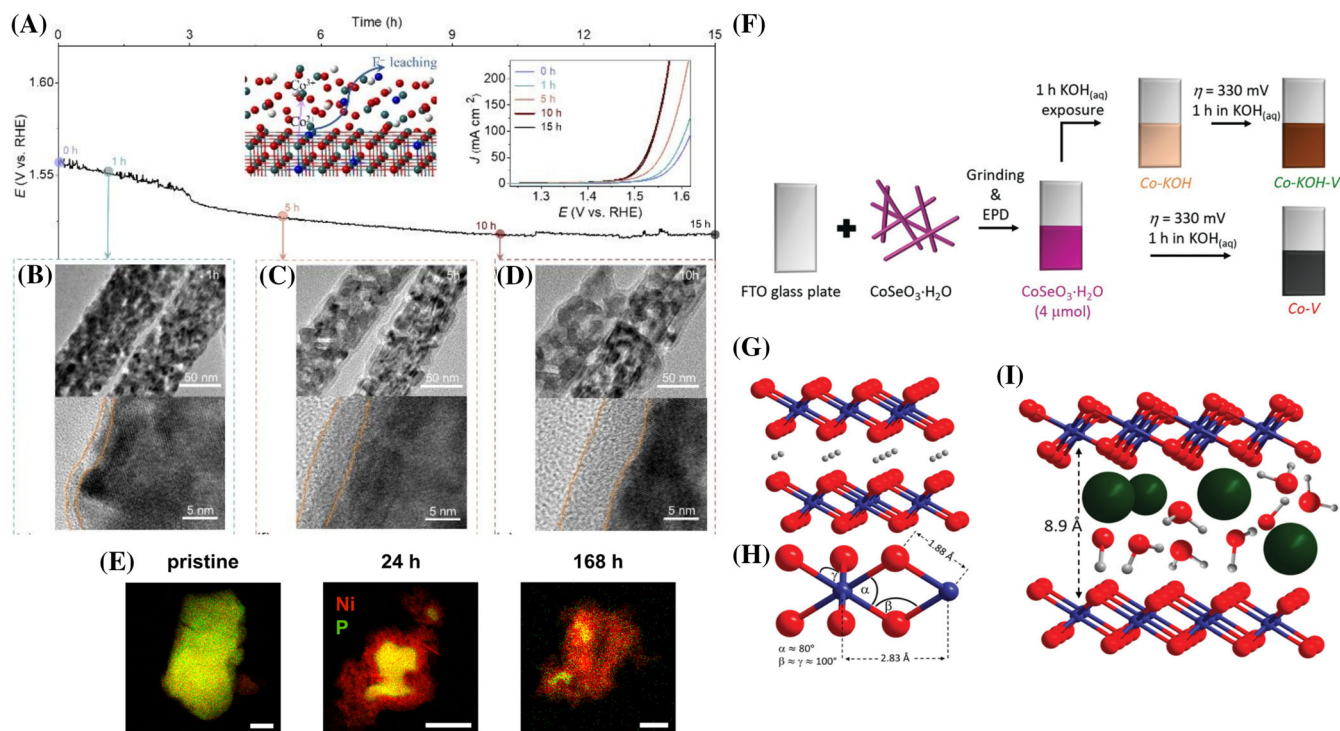


**FIGURE 11** (A) Chronopotentiometric curve obtained with the F-CoO/CC electrode with a positive current at a current density of 20 mA cm<sup>-2</sup>. The left inset is the illustrations of the F<sup>-</sup> leaching and the change of the Co valence state during the constant current anodization process. The right inset is the LSV curves with the increase of the constant current anodization time. TEM (top) and HRTEM (bottom) images of constant current anodization F-CoO/CC for (B) 1 h, (C) 5 h, and (D) 10 h. Reproduced with permission.<sup>104</sup> Copyright 2020, Royal Society of Chemistry. (E) EDS elemental maps with Ni (red), P (green), and O (blue) signals for sub-micrometer particles in pristine state and after 24 h as well as 168 h of chemical aging. Scale bars equal 100 nm. Reproduced with permission.<sup>105</sup> Copyright 2020, American Chemical Society. (F) Scheme of the deposition and the two herein presented transformation pathways with the names of the obtained compounds and intermediates. (G) Structure and layer stacking of β-CoOOH. (H) Structural motif of Co-V with distances obtained by EXAFS simulation and resulting bond angles. (I) Structural model of an area of Co-V with parallel domain stacking showing the layer distance in correct relation to interlayer K<sup>+</sup>, H<sub>2</sub>O, and HO<sup>-</sup>. Reproduced under a Creative Commons Attribution-NonCommercial 3.0 Unported License.<sup>106</sup> Copyright 2021, the Authors. Published by Royal Society of Chemistry.

The extent of leaching of the anions is crucial in determining the ultimate OER efficiency. In a report from the Mullins group, the sulfur anion in nickel sulfide was found to be totally depleted in the active nickel oxide electrocatalyst.<sup>103</sup> Later, the Zhang group reported an anion doping and leaching-induced amorphization strategy to optimize the OER performance.<sup>104</sup> With the increase of activation time, the ratio of F<sup>-</sup> decreased from ~5% at 1 h to ~3% at 10 h. The levels of F and Co<sup>3+</sup> stay constant between 10 and 15 h, suggesting that the surface reconstruction process may reach its peak after prolonged activation. (Figure 11A). The HRTEM image (Figure 11B–D) revealed that the growth of the amorphous shell ceased after 10 h of anodization and maintained a size of 7–8 nm after 15 h. This observation provides more evidence to support the conclusion that the leaching process is self-limiting. However, Masa et al. postulated an otherwise. They prolonged the anodization time up to 168 h on the Ni<sub>y</sub>P electrode and depicted a

composition evolution diagram after continuous chemical aging (Figure 11E).<sup>105</sup> Initially, a thin amorphous skin was already generated on the as-prepared material. During the process of aging, the release of phosphorus resulted in the generation of a core-shell heterostructure consisting of a core made of Ni<sub>y</sub>P, an intermediate layer of NiO, and an outer layer of Ni(OH)<sub>2</sub>. Upon further increasing the aging time, the complete oxidation led to a thick Ni(OH)<sub>2</sub> layer, which was detrimental for the activity.

What is the reason for the higher activity of (oxy) hydroxides produced by in situ anions leaching than the pristine ones? In this study, Driess et al. investigated a cobalt selenite pre-catalyst that underwent irreversible reconstruction into two distinct metal (oxy)hydroxides, depending on the pH and voltage.<sup>106</sup> As described in Figure 11F, three materials, Co-KOH, Co-KOH-V (as-synthesized (oxy)hydroxide), and Co-V ((oxy)hydroxide after leaching ions), were synthesized. From ICP-OES

results, selenium was depleted in all the three samples. By combining many characterizations, it was demonstrated that the Co-KOH-V catalyst exhibited catalytic activity in close proximity to the surface, while the other Co-V catalysts displayed catalytic activity from surface to bulk. Structure model obtained by EXAFS simulation indicated that the Co-KOH-V material exhibits significant domain size and a narrow layer spacing, whereas the Co-V material has smaller domains and a wider interlayer spacing. This structural difference allows for electrolyte penetration, hence facilitating the catalytic activity of the entire material (Figure 11G–I). Therefore, it can be inferred that the improved OER activity of the Co-V catalyst after removing anions is due to the significant reduction in size of the cobalt layers in the catalyst and the nano-template effect resulting from the quick formation and subsequent removal of  $(\text{Se}^{\text{VI}}\text{O}_4)^{2-}$ .

## 5 | ACTIVE COMPONENT LEACHING DURING OER

Apart from some specific examples in which the leached component would deposit back and participate in the formation of new active species, active component leaching generally represents the stability degradation of catalysts, which has been a key problem that should be addressed in acidic OER system.<sup>16,17,107</sup> This section initially presented several examples of leaching-redeposition. It then emphasized the advancements made in reducing leaching and enhancing the catalytic stability of noble-metal based materials in an acidic environment.

### 5.1 | Leaching-redeposition of active metal sites

Fe is widely recognized as a highly effective catalyst for alkaline OER, especially when it is added as a dopant to Ni/Co-based catalysts. Early in 1987, Corrigan et al. made the initial discovery that the presence of Fe impurities, whether injected from the electrolyte or coprecipitated into Ni (oxy)hydroxide, significantly reduced the reaction potential.<sup>108</sup> At elevated potentials, Fe undergoes oxidation to form  $\text{FeO}_4^{2-}$ , which is thermodynamically unstable as indicated by the Pourbaix diagram.<sup>26,109</sup> This instability causes the catalytic Fe centers to leach out over time, resulting in a degradation of the OER activity.

Remarkably, the Boettcher group systematically studied the OER behavior of Fe (oxy)hydroxides in KOH media.<sup>110</sup> At overpotentials below 0.35 V, the rate of iron leaching is minimal because only the first layer of the electrolyte-permeable iron oxyhydroxide participates in

the OER. At increasing overpotentials, the conductivity of  $\text{FeOOH}$  increases, causing a greater portion of the catalyst film that allows the passage of electrolyte to participate in OER catalysis. This leads to an increase in the dissolution rate (creation of soluble  $\text{FeO}_4^{2-}$ ) of the  $\text{FeOOH}$  film. Following these observations, the Li group achieved good stability for the NiFe-LDH catalysts via a self-healing route.<sup>111</sup> It is found that Co will promote the Fe redeposition under anodic potentials. A material called NiCoFe-LKD was created and exhibited consistent performance in the OER for a duration of 1000 h. This indicates that the process of removing and redepositing the catalytic centers achieved a state of balanced and continuous activity in the OER environment. A study conducted by the Markovic group revealed that the OER activity of Sr-doped  $\text{LaCoO}_3$  particles is attributed to a Co hydro(oxy)oxide ( $\text{CoO}_x\text{H}_y$ ) layer that is only a few nanometers thick. This layer interacts with trace-level Fe (aq) in the KOH electrolyte, resulting in the formation of dynamically stable active sites.<sup>112</sup> A dynamic equilibrium between Fe leaching and redeposition is established during OER. Additionally, the strong contact between Fe and  $\text{CoO}_x\text{H}_y$  helps to keep a significant number of Fe sites at the interface, which enhances the OER rates (Figure 12A). This dynamic equilibrium was also demonstrated by isotopic label experiments.

Noble metal-based materials have been the top choices for water oxidation in acidic media as most transition metals are unstable in acidic environment. Following the pioneering study of perovskite  $\text{SrIrO}_3$  catalyst in acidic OER, the Grimaud group investigated the catalytic behaviors of double perovskite  $\text{Sr}_2\text{M}(\text{V})\text{O}_6$  ( $\text{M} = \text{Fe}, \text{Co}$ ) and Ruddlesden–Popper (RP) structured  $\text{Sr}_2\text{Fe}_{0.5}\text{Ir}_{0.5}(\text{V})\text{O}_4$ .<sup>113</sup> Leaching of alkaline metal as well as the dissolution of Ir were observed by ICP measurements. The researchers suggested a dissolution-electrodeposition/precipitation pathway as the origin of the OER activity in these perovskites. As illustrated in Figure 12B, all the catalysts suffered from Ir leaching when immersing into the acidic electrolyte and the leached Ir species subsequently electrodeposited as  $\text{IrO}_x \cdot m\text{H}_2\text{O}$  on the perovskite surface to give rise to the OER activity. Figure 12C shows the experimental reconstruction of the iridium Pourbaix diagram, which will aid future studies aimed at designing more efficient Ir-based OER catalysts by regulating the dissolution/precipitation equilibrium of iridium species.

Dynamic leaching-redeposition is an interesting behavior. All catalysts undergo a dynamic leaching-redeposition route would form an amorphous layer on their surface. It appears that the catalyst will heal itself through this process. However, when the catalyst is applied to a flowing electrolyzer, the dissolved ions may not be able to be redeposited, resulting in a loss of active

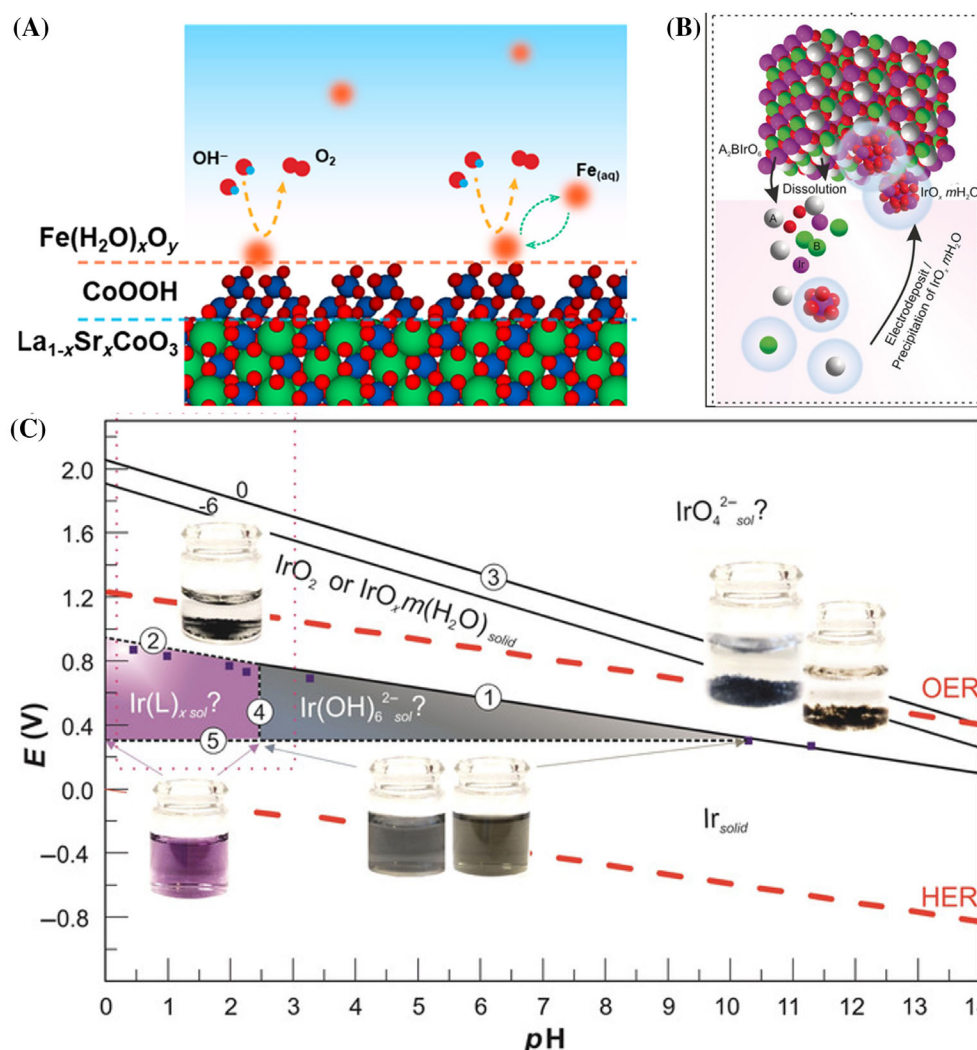


**FIGURE 12** (A) Schematic of the multilayered core-shell interface formed over a surface evolved LSCO perovskite oxide, highlighting the Fe active sites that are dynamically stable due to strong interaction with CoOOH surface species. Reproduced with permission.<sup>112</sup> Copyright 2021, American Chemical Society. (B) The proposed OER catalytic mechanism involving the dissolution-electrodeposition of iridium species. (C) Iridium E<sub>H</sub>-pH diagram. Reproduced with permission.<sup>113</sup> Copyright 2019, Wiley-VCH.

sites. This is a scientific question worth thinking about and studying.

## 5.2 | Strategies to suppress active component leaching in acidic OER

Developing efficient OER electrocatalysts in acidic condition is critically important for practical application of proton exchange membrane (PEM) electrolyzers.<sup>114–116</sup> For a long time, only Ir and Ru based catalysts have been studied due to their intrinsic characters and relatively higher stability in acidic media than transition metals. However, in acidic OER, soluble RuO<sub>4</sub>/IrO<sub>4</sub> species are still easily formed, leading to poor stability.<sup>117,118</sup> Thus, much efforts have been made to suppress the active component

leaching when designing efficient Ru/Ir-based catalysts for acidic OER. Generally, the representative strategies are loading on appropriate support materials, tuning composition or crystal facet of catalysts, engineering electronic property of catalysts and suppressing lattice oxygen participation.

### 5.2.1 | Loading on appropriate support materials

An ideal support material needs to be tolerant to corrosion and has strong interaction with the supported materials. In 2016, the Strasser group first demonstrated the existence of metal/metal-oxide support interactions (MMOSI) in IrO<sub>x</sub>-supported oxide systems.<sup>119</sup> As uncovered



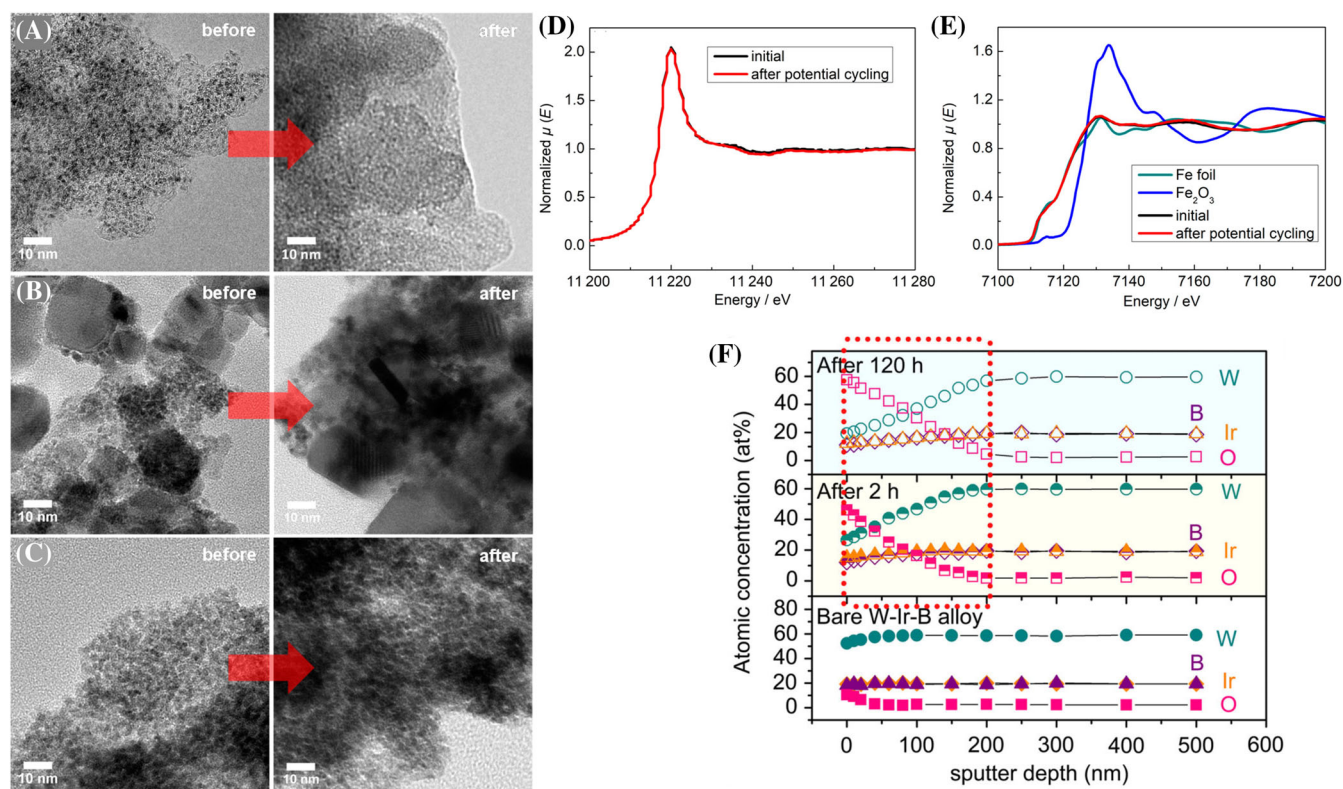


**FIGURE 13** TEM images of (A)  $\text{IrO}_x/\text{C}$ , (B)  $\text{IrO}_x/\text{Com}$ , ATO, and (C)  $\text{IrO}_x/\text{ATO}$  electrocatalysts before and after stability test (Chronopotentiometry at  $1 \text{ mA cm}^{-2}$ , for 15 h). Reproduced with permission.<sup>119</sup> Copyright 2016, American Chemical Society. (D) XANES spectra of Ir-L<sub>3</sub> edge for  $\text{Ir-SA@Fe@NCNT}$  at the initial state and after potential cycling. (E) XANES spectra of Fe-K edge for  $\text{Ir-SA@Fe@NCNT}$  at the initial state and after potential cycling. Reproduced with permission.<sup>121</sup> Copyright 2020, American Chemical Society. (F) XPS sputter depth profile measurements of the bare W-Ir-B alloy catalyst, the alloy catalyst after 2 h OER test, and the alloy catalyst after 120 h OER test. The red dotted box indicates the depth of the surface active thin layer. Reproduced under the terms of the Creative Commons CC-BY License.<sup>122</sup> Copyright 2021, the Authors. Published by Nature Publishing Group.

by the TEM images of  $\text{IrO}_x/\text{ATO}$ ,  $\text{IrO}_x/\text{C}$  and  $\text{IrO}_x/\text{Com}$ . ATO electrodes before and after stability test in acidic electrolyte (Figure 13A–C), the  $\text{IrO}_x/\text{ATO}$  catalysts showed no significant differences, while the carbon support corroded and collapsed in the  $\text{IrO}_x/\text{C}$  catalyst. After stability test, the mass loss percentage of Ir in  $\text{IrO}_x/\text{ATO}$  was calculated to be 28.3%, while for  $\text{IrO}_x/\text{C}$ , it was 97.1%. These suggest that the MMOSI effect would suppress Ir leaching, thus maintaining the high charge-transfer kinetics. Inspired by this, Reek et al. developed isolated Ir atoms derived from a molecular Ir complex that can be selectively anchored on manganese oxide.<sup>120</sup> Compared to the material produced from  $\text{H}_2\text{IrCl}_6$ , the novel  $\text{Ir-MnO}_x/\text{NC}$  electrode shows more active and more stable catalytic behavior, without suffering from Ir leaching, which demonstrates the critical role of a stable Ir precursor. Very recently, the Cai group realized robust water splitting in acid using a double protecting strategy through dispersing atomic Ir on Fe nanoparticles and implanting IrFe into nitrogen-doped carbon nanotubes.<sup>121</sup> During the 12-h OER operation, little degradation was

observed. Ex situ Ir-L<sub>3</sub> and Fe-K edge XANES spectra before and after potential cycling were collected to illustrate such robust stability. As uncovered by Figure 13D,E, both coordination environment and oxidation state of Ir and Fe were essentially maintained, which can be ascribed to the double protecting strategy. Furthermore, the Xiong group focused on metal tungsten (W) and studied the MMOSI effect that balance the OER stability and activity.<sup>122</sup> IrW-W<sub>2</sub>B (W-Ir-B) alloy was first fabricated and the active IrW nanochannel layer emerged as efficient and ultra-stable OER catalyst after the selective corrosion on W<sub>2</sub>B. Figure 13F depicts the Ir, W, B and O XPS depth profiles before and after OER. It is explicit that the tested elements have no significant leaching even after 120-h operation, indicating the robust stability during long-term test. Combined with other characterizations and theoretical calculations, it is unveiled that the IrW support not only confines the size of surface Ir oxide cluster, but also engineer charge distribution of Ir, which help to prevent surface Ir from agglomeration and reduce Ir valence to avoid its over-oxidation, respectively.



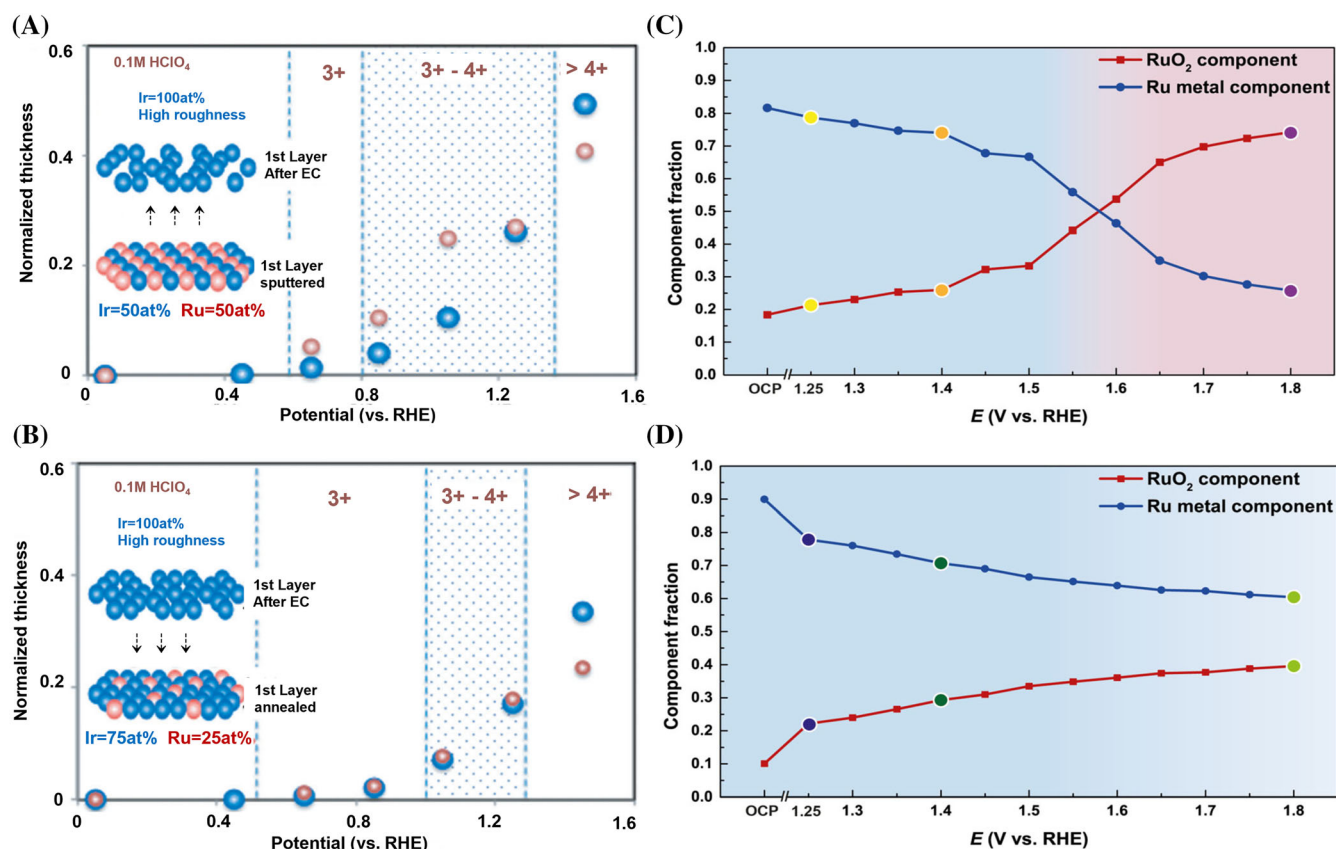


**FIGURE 14** The potential-dependent changes in the valence states of (A) sputtered and (B) annealed Ru<sub>0.5</sub>Ir<sub>0.5</sub>, as determined from XANES analyses. Reproduced with permission.<sup>123</sup> Copyright 2014, Wiley-VCH. Linear composition fitting (LCF) results using two components, Ru metal and RuO<sub>2</sub> in the XANES spectra of (C) RuIr-NS and (D) RuIr-NC collected by *operando* tests. Reproduced under a Creative Commons Attribution 4.0 International License.<sup>125</sup> Copyright 2021, the Authors. Published by Nature Publishing Group.

### 5.2.2 | Tuning composition or crystal facet of catalysts

Considering that Ru based materials usually exhibit higher activity but poorer stability compared to Ir based counterparts, much efforts have been dedicated to pursuing activity-stability optimization focusing on Ru-Ir bimetallic catalysts. In 2014, the Markovic group successfully tuned the near-surface composition of catalyst using a new “surface segregation” strategy.<sup>123</sup> The resultant catalyst (annealed Ru<sub>0.5</sub>Ir<sub>0.5</sub>) realized high intrinsic activity as well as long stability for OER. As observed from Figure 14A,B, the thickness of Ir oxide with valence state of more than +4 is larger than Ru oxides. Besides optimizing catalyst composition, Zou et al. designed a 6H-SrIrO<sub>3</sub> perovskite catalyst with highly active and stable performance by constructing the face-sharing IrO<sub>6</sub> octahedral subunits.<sup>124</sup> The face-sharing IrO<sub>6</sub> dimers have obvious weaker Ir—O bonds compared to the corner-shared rutile IrO<sub>2</sub>, thus ensuring less surface amorphourization or structure loss during OER catalysis. As implied from the ICP-OES

results, the Ir species in 6H-SrIrO<sub>3</sub> leached much less than that of the conventional rutile IrO<sub>2</sub>, indicating its remarkable structural stability. Following the previous studies, Kitagawa et al. developed a solid-solution Ru-Ir nanosized-coral (RuIr-NC) catalyst which shows outstanding OER activity for 122 h without noticeable degradation.<sup>125</sup> In contrast, the spherical counterpart has degradable behavior within 1 h. Figure 14C and Figure 14D recorded the percentages of Ru and RuO<sub>2</sub> components as a function of applied bias for the RuIr-NC and RuIr-NS electrodes, respectively. Only ~25% metallic component in the RuIr-NS remained at 1.8 V, while for the RuIr-NC, nearly 60% metallic component was maintained. Similar results were obtained on metal Ir for the two catalysts. These indicate that both Ru and Ir in the RuIr-NC are more resistant to oxidation compared with those in the RuIr-NS. Combined with other characterizations, the preferentially exposed extended [0001] facet of the RuIr-NC electrode was revealed to be the exclusive factor that suppress the generation of dissolvable metal oxides, making it a long-lived OER catalyst.

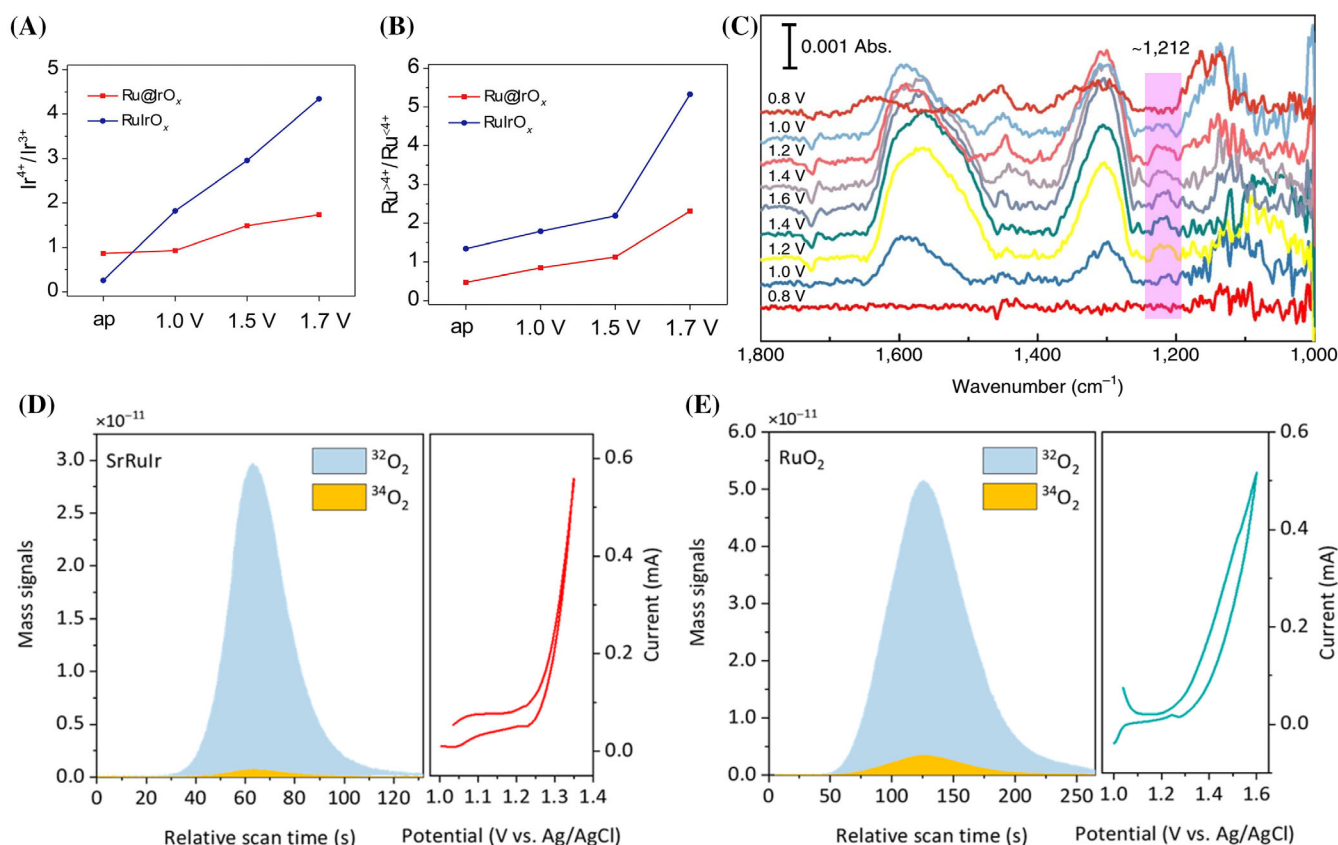


**FIGURE 15** (A)  $\text{Ir}^{4+}/\text{Ir}^{3+}$  and (B)  $\text{Ru}^{4+}/\text{Ru}^{3+}$  ratio curve obtained for  $\text{Ru@IrO}_x$  and  $\text{RuIrO}_x$  electrocatalysts before OER (the as-prepared samples, which are denoted as “ap”) and after polarizing at different potentials. Reproduced with permission.<sup>129</sup> Copyright 2019, Elsevier Inc. (C) In situ ATR-IR spectra recorded during the multi-potential steps. Reproduced with permission.<sup>128</sup> Copyright 2019, Nature Publishing Group. DEMS signals of  $^{32}\text{O}_2$  ( $^{16}\text{O}^{16}\text{O}$ ) and  $^{34}\text{O}_2$  ( $^{16}\text{O}^{18}\text{O}$ ) from the reaction products for  $^{18}\text{O}$ -labeled (D)  $\text{SrRuIr}$  and (E)  $\text{RuO}_2$  catalysts in  $\text{H}_2^{18}\text{O}$  aqueous sulfuric acid electrolyte and corresponding CV cycles. Reproduced with permission.<sup>131</sup> Copyright 2021, American Chemical Society.

### 5.2.3 | Engineering electronic property of catalysts

Constructing heterostructure with electron redistribution across the interface to suppress metal over-oxidation has been investigated as another efficient method to optimize the leaching resistance of catalysts.<sup>126,127</sup> In 2019, the Li group synthesized a series of Pt-Cu alloys with embedded Ru atoms for acidic OER, in which the best catalyst  $\text{Ru}_1\text{-Pt}_3\text{Cu}$  delivered remarkable activity.<sup>128</sup> The compressive strain of the Pt shell was found to tune the electronic structure and oxidation state of Ru single atom, thus suppressing over-oxidation of Ru and optimizing the binding of oxygen intermediates simultaneously. Another report by the Qiao group obtained similar conclusion. They designed a hetero-structured  $\text{Ru@IrO}_x$  catalyst in which a strong charge redistribution exists between Ru core and Ir oxide shell.<sup>129</sup> Figure 15A,B plots the  $\text{Ir}^{4+}/\text{Ir}^{3+}$  and  $\text{Ru}^{4+}/\text{Ru}^{3+}$  ratios, respectively, of the  $\text{RuIrO}_x$  and  $\text{Ru@IrO}_x$  electrodes under operating potentials.

Obviously, the valence of Ru in  $\text{Ru@IrO}_x$  is always lower than that in  $\text{RuIrO}_x$ , and the  $\text{Ir}^{4+}/\text{Ir}^{3+}$  value in  $\text{Ru@IrO}_x$  has little change during the catalysis process. These confirm that the charge redistribution at the core-shell heterojunction leads to the reduced metal leaching rates. In addition, Deng et al. reported robust interface Ru centers between  $\text{RuO}_2$  and graphene in acidic OER.<sup>130</sup> It was confirmed that the electron-rich interface could act as an electron reservoir to donate electrons to the  $\text{RuO}_2$ , preventing the over-oxidation and leaching of  $\text{RuO}_2$ .

### 5.2.4 | Suppressing lattice oxygen participation

During the acidic OER, Ru based catalysts usually suffer from the participation of lattice oxygen which would easily result in the collapse of the catalyst structure, thus accelerating the dissolving of active Ru species. In this regard, changing the dominant  $\text{O}_2$  evolution pathway

from LOM to AEM should be an effective method to suppress the Ru dissolution during the OER. In the case of the durable Ru<sub>1</sub>-Pt<sub>3</sub>Cu catalyst mentioned above, the oxidation state of Ru kept almost unchanged in the OER condition.<sup>128</sup> As shown in Figure 15C, the peak located at approximately 1212 cm<sup>-1</sup> can be ascribed to the surface-adsorbed superoxide (OOH<sub>ad</sub>). This confirms that AEM rather than LOM mechanism dominated the O<sub>2</sub> generation on Ru<sub>1</sub>-Pt<sub>3</sub>Cu catalyst surface, guaranteeing the catalytic stability during the acidic OER. Moreover, the Sargent group realized a dual-modulation strategy to suppress the lattice oxygen oxidation mechanism (LOM) and tune the activity of Ru sites.<sup>131</sup> The best-performing SrRuIr oxide electrode optimized by DFT screening achieved 10 mA cm<sup>-2</sup> at a low overpotential of 190 mV and such performance has no obvious deactivation in the following 1500 h. EXAFS spectra of the Ru K-edge and Ir L<sub>3</sub>-edge indicated the increased bond length of Ru—O and slightly decreased Ir—O bond length in the SrRuIr compared with that in pristine RuO<sub>2</sub> and IrO<sub>2</sub>, respectively, indicating the interaction among Ru, Ir and O. Furthermore, in situ differential electrochemical mass spectroscopy (DEMS) measurements using isotope <sup>18</sup>O were carried out for detecting lattice oxygen in OER. Before the experiments, The catalyst surface was generally labeled with <sup>18</sup>O. As uncovered by Figure 15D,E, the <sup>34</sup>O<sub>2</sub> generated on SrRuIr surface is much lower than that on RuO<sub>2</sub>. After calculation, compared to the RuO<sub>2</sub>, the LOM pathway on SrRuIr is suppressed by ~50%, and most of the generated O<sub>2</sub> was evolved via AEM pathway. These suggest that the strong interaction in the Ru-O-Ir structure would reduce the lattice oxygen involvement during OER, thus suppressing the decay of the catalyst.

Currently, only the precious metal Ir can be successfully commercialized in PEM-based electrolyzers. Despite the many attractive advantages of ion leaching, the leaching of the precious metal Ir is something we do not want. Therefore, inhibiting the dissolution of Ir has great

practical value. As a potential substitute for Ir, Ru is more abundant, cheaper, and has higher OER activity, but it is less stable and easier to leach. In the future, if the dissolution of Ru in the OER process can be successfully suppressed, the cost of hydrogen production from PEM can be greatly reduced.

## 6 | THE DISCUSSION OF LEACHING EFFECT ON WATER OXIDATION

Based on the above research progresses, we can find that leaching affects the catalysts in many aspects and eventually determines the performance of water oxidation. This section will systematically discuss the leaching effect on water oxidation, including both positive and negative impacts (Figure 16). How to promote the positive effects while suppress the negative ones was briefly introduced at the end of each part.

### 6.1 | Positive effect

The intuitive advantage of leaching inactive components lies in its ability to eliminate unwanted species, introduce defects, and augment the number of active sites for water oxidation. The profound efficacy of this process, as revealed by in situ techniques, extends to the acceleration of surface reconstruction in electrocatalysts, leading to the formation of nanoscale morphologies and unconventional electronic and geometric structures. These newly formed features exhibit enhanced water oxidation activity and stability. Furthermore, the leaching of even active components can be advantageous for water oxidation through a leaching-redeposition mechanism, a prevalent method of surface reconstruction. This dynamic leaching-redeposition cycle preserves the surface-active

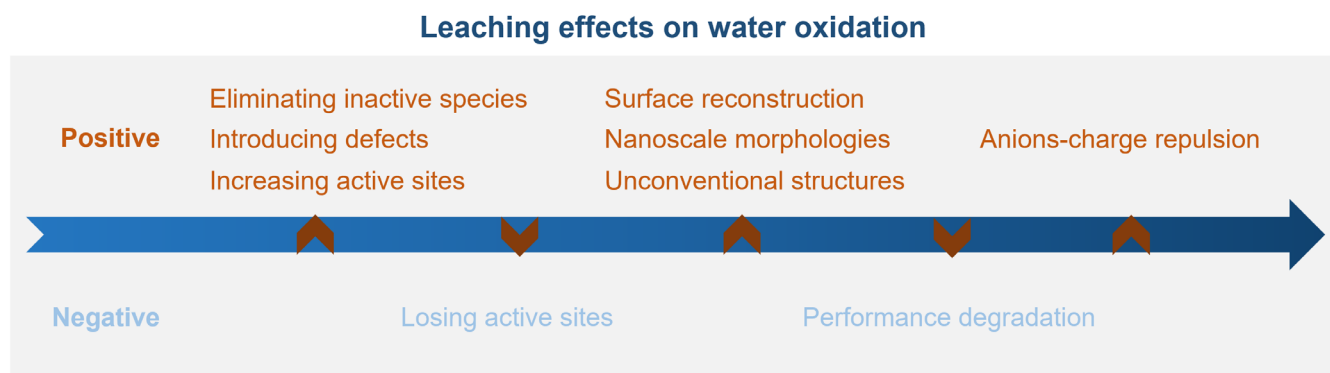


FIGURE 16 The leaching effects on water oxidation.



species. Ultimately, anion leaching is recognized for its beneficial impact on seawater oxidation. The oxidation of chloride ions ( $\text{Cl}^-$ ) is a significant side reaction in seawater oxidation, posing severe stability challenges. As discussed in Section 4.6, the anions in the materials would transform into their corresponding oxyanions during the OER. The presence of these negatively charged oxyanions impedes the adsorption of  $\text{Cl}^-$  on the electrode surface due to electrostatic repulsion of like charges, thereby preventing the involvement of  $\text{Cl}^-$  in seawater oxidation and enhancing the process's overall stability.

Tips for how to promote the positive effects of leaching: (i) Introducing metastable elements around the active sites; (ii) Finely manipulating the electrochemical methods/parameters and treatment times; and (iii) Always referring the Pourbaix diagram before conducting research.

## 6.2 | Negative effect

In addition to outlining the benefits of ion leaching, this paper also sheds light on its detrimental impacts on the activity and stability of water oxidation catalysts, with the primary concern being the leaching of active components. A notable example is the leaching of iridium (Ir) and ruthenium (Ru) under acidic conditions. Driven by strong oxidation potentials, the Ir and Ru centers can be oxidized into their high-valence and soluble forms,  $\text{IrO}_2-4$  and  $\text{RuO}_2-4$ , respectively. This results in the loss of active sites, leading to a natural decline in both activity and stability.

Strategies to suppress the leaching of Ir/Ru were discussed in the section of 5. Now we introduce a possible direction for suppressing the negative effects of leaching, that is, coating a thin-layer of mixed ion-conductor which allows the transport of  $\text{OH}^-/\text{H}^+$  and suppresses the leaching of Ir/Ru.

## 7 | CONCLUSIONS AND PERSPECTIVE

Component leaching of electrocatalysts is a common phenomenon during OER. Systematic understanding of the key origins, distinct behaviors and induced effects regarding leaching is critical toward design and prediction of next-generation catalysts with better durability and activity. In the first section of this review, we reveal the origin of element leaching with the help of Pourbaix diagram, which supplies a convincing rule to predict the stability of a catalyst in its working condition. Afterward, advanced microscopy, spectroscopic and other characterization methods are introduced to analyze the variation of catalysts in morphology, structure, composition, electronic configuration and so on, which is induced by the component leaching during the OER. In particular, the emerging *in situ/operando* methodologies are highly desired for capturing the dynamic changes of catalysts under OER conditions, so as to push forward the understanding of leaching process. In the next section, we focus on the inactive component leaching of catalysts during OER. According to the unique structure and property of each category of OER catalysts, their distinct leaching behaviors and the induced effects are discussed in detail. The last part relates to the active component leaching under OER condition. Apart from some specific species that are capable of leaching and redeposition, this generally represents stability degradation of catalysts and often occurs on noble-element electrodes in acidic OER. In this regard, progress in suppressing leaching and improving catalytic stability of Ru/Ir based catalysts in acidic environment are highlighted. Here we summarize three representative types of structure transformation induced by leaching metastable species under OER condition. In the first circumstance, the structure of a pristine catalyst

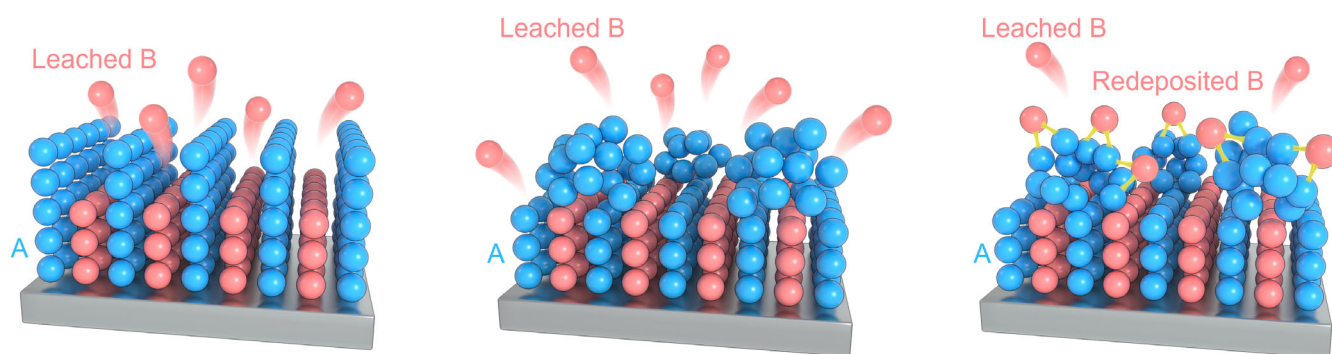


**FIGURE 17** Proposed three representative types of structure transformation induced by leaching of metastable species in OER condition. (i—left) well maintained structure (ii—middle) collapse of initial crystalline lattice and (iii—right) interaction between leached ions and the substrate.

(Figure 17A) would be well maintained after the leaching of unstable component. Under the second condition, the substantial element leaching from crystals would lead to the collapse of the initial crystalline lattice as schematically illustrated in Figure 17B. The third situation mainly refers to leaching-redeposition, in which the easily dissolved elements would selectively redeposit on the catalyst surface (Figure 17C). In general, the leached component serves as sacrificial template and dissolve, introducing large amount of voids, thus exposing more active sites in the catalyst. The remaining structure with rich pores or channels would enhance the mass transfer and thus the electrocatalytic kinetics during the electrochemical reactions. Moreover, the defects or vacancies created by leaching could modulate electronic configurations of the remaining catalyst structure, which would adjust the adsorption energy during reaction and improve the catalytic performance. Particularly, resulting from the electrostatic interaction, the leached anions would be possibly captured by the catalyst surface under anodic bias, and the interaction between anions and the substrate would promote the OER behavior. Although visible progress has been made up to now, plenty of issues still remain to be addressed:

### 7.1 | More accurate characterizations on leaching

Besides the commonly used techniques, more advanced characterizations are required to gain more insights in the leaching process during OER. For instance, the scanning electrochemical microscopy (SECM) could establish a favorable interface between electrochemistry to microscopy, enabling the possibility of high-resolution electrochemical testing, monitoring the electrochemical reactions occurring in the far-field region (from a few nanometers to a few microns above the outermost surface of catalyst). Moreover, the liquid-phase TEM technique needs to be further optimized so as to gain easy access to “see” the morphology change and crystal lattice evolution at atomic level in real-time.

### 7.2 | Optimal activation method for accelerating leaching process

Typically, the as-prepared OER catalysts would undergo an “activation process” to achieve their real catalytic performance. Component leaching usually takes place during such process. The most frequently used methods are CV, chronopotentiometric (CP), and chronoamperometric (CA) measurements, in which the CV method is a continuous redox process while the other two are

carried out under a fixed potential or current density. This may lead to difference in the leaching behavior of catalysts, thus affecting the final performance. It is highly desirable to select optimal activation method for accelerating leaching process according to the distinct properties of the unstable species in the pre-catalysts. Therefore, systematic studies are urgent to reveal the relationships between the degree of leaching and the electrochemical method used.

### 7.3 | Systematically studying the effects of leaching level/depth on the catalytic behavior

OER is a typical heterogeneous electrocatalytic process which generally happens on the catalyst surface. Therefore, the OER behavior is mainly dominated by the character of the newly exposed surface after component leaching. Also, the interface between the newly formed species and the remained part have great influences in the desorption/adsorption of reaction intermediates as well as the electrons/ions transfer when catalyzing OER. Considering these aspects, it is important to systematically investigate the effect of leaching level/degree when growing new species at the surface as well as the interfacial effect at the interface (oxyhydroxide/oxide-core/shell catalysts derived from perovskite materials), so as to have the largest performance improvement for OER systems.

### 7.4 | Deeper understanding of the anion leaching effect on OER performance

Usually, we tacitly assume that the anions leached from polyoxometalate material or anion-decorated metal compounds will be dissolved into the electrolyte. It is the remaining structure that participates in catalyzing the OER. However, results from the latest studies have challenged this viewpoint. For example, the dissolved  $\text{SO}_4^{2-}$  in the electrolyte was found more easily captured by Ni site of the NiFe (oxy)hydroxide catalyst, and the surface-adsorbed  $\text{SO}_4^{2-}$  was demonstrated to lead to the OER activity improvement. Another study revealed the surface-adsorbed selenite by in situ Raman, and it was confirmed that the surface-adsorbed selenate could promote the OER activity. Theoretically, when an oxidation potential is applied during OER, it is possible for the anions dissolved in electrolyte to adsorb on the electrode due to electrostatic interaction, which would probably provide new insights in the structure evolution after anion leaching and renew the “electronic structure-catalytic behavior” relation.

## 7.5 | Predicting the electrochemical stability of complex materials by utilizing computational simulations

From the electrode potential-pH (Pourbaix) diagram, we can easily predict the most stable species in aqueous condition. From recent studies, it is challenging to perform Pourbaix analysis when analyzing multidimensional systems given the high-throughput material exploration and complexity increase in materials for electrochemical applications. To predict the aqueous stability of catalysts more accurately, appropriate functionals (such as the strongly constrained and appropriately normed [SCAN] functional) could be employed when constructing the Pourbaix diagram for complex materials. Moreover, the Pourbaix analysis of complex materials in OER system is particularly valuable for developing strategies for promoting/suppressing leaching of catalyst component during OER. For example, it can be applied to predict the leaching potentials of the target catalysts in acidic OER.

### ACKNOWLEDGMENTS

This work was supported by the Program for Jiangsu Specially-Appointed Professors (R2023T05, YQR23123) and the Startup Foundation for Introducing Talent of NUIST (2024R078). This work was also supported by the Hong Kong Polytechnic University (1-WZ5L, Q-CDBG, and 1-ZE2F).

### CONFLICT OF INTEREST STATEMENT

The authors declare no conflicts of interest.

### ORCID

Gao Chen  <https://orcid.org/0000-0001-6561-4167>

Hainan Sun  <https://orcid.org/0000-0003-1589-3860>

Haitao Huang  <https://orcid.org/0000-0002-3861-2702>

### REFERENCES

1. Tollefson J. Can the world kick its fossil-fuel addiction fast enough? *Nature*. 2018;556(7702):422-426.
2. De Luna P, Hahn C, Higgins D, Jaffer SA, Jaramillo TF, Sargent EH. What would it take for renewably powered electrosynthesis to displace petrochemical processes? *Science*. 2019;364(6438):eaav3506.
3. Tang J, Su C, Shao Z. Advanced membrane-based electrode engineering toward efficient and durable water electrolysis and cost-effective seawater electrolysis in membrane electrolyzers. *Exp Dermatol*. 2024;4(1):20220112.
4. Sun H, Xu X, Kim H, Shao Z, Jung W. Advanced electrocatalysts with unusual active sites for electrochemical water splitting. *InfoMat*. 2024;6(1):e12494.
5. She ZW, Kibsgaard J, Dickens CF, Chorkendorff IB, Nørskov JK, Jaramillo TF. Combining theory and experiment in electrocatalysis: insights into materials design. *Science*. 2017;355(6321):eaad4998.
6. Li L, Chen G, Shao Z, Huang H. Progress on smart integrated systems of seawater purification and electrolysis. *Energ Environ Sci*. 2023;16(11):4994-5002.
7. Sun H, Xu X, Kim H, Jung W, Zhou W, Shao Z. Electrochemical water splitting: bridging the gaps between fundamental research and industrial applications. *Energ Environ Mater*. 2023;6(5):e12441.
8. Chen RR, Chen G, Ren X, et al. SmCo<sub>5</sub> with a reconstructed oxyhydroxide surface for spin-selective water oxidation at elevated temperature. *Angew Chem Int Ed*. 2021;60(49):25884-25890.
9. Yu ZY, Duan Y, Feng XY, Yu X, Gao MR, Yu SH. Clean and affordable hydrogen fuel from alkaline water splitting: past, recent progress, and future prospects. *Adv Mater*. 2021;33(31):2007100.
10. Li Y, Chen G, Chen HC, et al. Tailoring the surface cation configuration of Ruddlesden-Popper perovskites for controllable water oxidation performance. *Energ Environ Sci*. 2023;16(8):3331-3338.
11. Zhu Y, Chen HC, Hsu CS, et al. Operando unraveling of the structural and chemical stability of P-substituted CoSe<sub>2</sub> electrocatalysts toward hydrogen and oxygen evolution reactions in alkaline electrolyte. *ACS Energy Lett*. 2019;4(4):987-994.
12. Zhu Y, Chen G, Zhong Y, et al. A surface-modified antiperovskite as an electrocatalyst for water oxidation. *Nat Commun*. 2018;9(1):2326.
13. Chen G, Zhu Y, Chen HM, et al. An amorphous nickel-iron-based electrocatalyst with unusual local structures for ultrafast oxygen evolution reaction. *Adv Mater*. 2019;31(28):1900883.
14. Zhu C, Shi Q, Feng S, Du D, Lin Y. Single-atom catalysts for electrochemical water splitting. *ACS Energy Lett*. 2018;3(7):1713-1721.
15. Wang Y, Liu B, Shen X, et al. Engineering the activity and stability of MOF-nanocomposites for efficient water oxidation. *Adv Energy Mater*. 2021;11(16):2003759.
16. Li L, Wang P, Shao Q, Huang X. Recent progress in advanced electrocatalyst design for acidic oxygen evolution reaction. *Adv Mater*. 2021;33(50):2004243.
17. Gao J, Tao H, Liu B. Progress of nonprecious-metal-based electrocatalysts for oxygen evolution in acidic media. *Adv Mater*. 2021;33(31):2003786.
18. Zhu Y, Kuo TR, Li YH, et al. Emerging dynamic structure of electrocatalysts unveiled by in situ x-ray diffraction/absorption spectroscopy. *Energ Environ Sci*. 2021;14(4):1928-1958.
19. Zhu Y, Wang J, Chu H, Chu YC, Chen HM. In situ/operando studies for designing next-generation electrocatalysts. *ACS Energy Lett*. 2020;5(4):1281-1291.
20. Zhu Y, Chen G, Chu YC, et al. Hetero-atomic pairs with a distal Fe<sup>3+</sup>-site boost water oxidation. *Angew Chem Int Ed*. 2022;61(48):e202211142.
21. Gao L, Cui X, Sewell CD, Li J, Lin Z. Recent advances in activating surface reconstruction for the high-efficiency oxygen evolution reaction. *Chem Soc Rev*. 2021;50(15):8428-8469.



22. Jiang H, He Q, Zhang Y, Song L. Structural self-reconstruction of catalysts in electrocatalysis. *Acc Chem Res.* 2018;51(51):2968-2977.
23. Li Y, Du X, Hung J, et al. Recent progress on surface reconstruction of earth-abundant electrocatalysts for water oxidation. *Small.* 2019;15(35):1901980.
24. Liu J, Guo L. In situ self-reconstruction inducing amorphous species: a key to electrocatalysis. *Matter.* 2021;4(9):2850-2873.
25. Zeng Y, Zhao M, Huang Z, et al. Surface reconstruction of water splitting electrocatalysts. *Adv Energy Mater.* 2022;12(33):2201713.
26. Pourbaix M. Applications of electrochemistry in corrosion science and in practice. *Corros Sci.* 1974;14(1):25-82.
27. Patel AM, Nørskov JK, Persson KA, Montoya JH. Efficient Pourbaix diagrams of many-element compounds. *Phys Chem Chem Phys.* 2019;21(45):25323-25327.
28. Wang Z, Zheng YR, Montoya J, et al. Origins of the instability of nonprecious hydrogen evolution reaction catalysts at open-circuit potential. *ACS Energy Lett.* 2021;6(6):2268-2274.
29. Wang Z, Zheng YR, Chorkendorff I, Nørskov JK. Acid-stable oxides for oxygen electrocatalysis. *ACS Energy Lett.* 2020;5(9):2905-2908.
30. Wang Z, Guo X, Montoya J, Nørskov JK. Predicting aqueous stability of solid with computed Pourbaix diagram using SCAN functional. *NPJ Comput Mater.* 2020;6(1):160.
31. Singh AK, Zhou L, Shinde A, et al. Electrochemical stability of metastable materials. *Chem Mater.* 2017;29(23):10159-10167.
32. Zhu Y, Chen G, Xu X, Yang G, Liu M, Shao Z. Enhancing electrocatalytic activity for hydrogen evolution by strongly coupled molybdenum nitride@ nitrogen-doped carbon porous nano-octahedrons. *ACS Catal.* 2017;7(5):3540-3547.
33. Chu YC, Chang CJ, Zhu Y, et al. Anionic effects on metal pair of Se-doped nickel diphosphide for hydrogen evolution reaction. *ACS Sustain Chem Eng.* 2019;7(16):14247-14255.
34. Vasileff A, Zhu Y, Zhi X, et al. Electrochemical reduction of CO<sub>2</sub> to ethane through stabilization of an ethoxy intermediate. *Angew Chem Int Ed.* 2020;132(44):1981719821.
35. Weber T, Pfrommer J, Abb MJS, et al. Potential-induced pitting corrosion of an IrO<sub>2</sub> (110)-RuO<sub>2</sub> (110)/Ru (0001) model electrode under oxygen evolution reaction conditions. *ACS Catal.* 2019;9(7):6530-6539.
36. Song CW, Suh H, Bak J, Bae HB, Chung SY. Dissolution-induced surface roughening and oxygen evolution electrocatalysis of alkaline-earth iridates in acid. *Chem.* 2019;5(12):3243-3259.
37. Chen G, Zhu Y, Ying Y, et al. Isolated active sites in perovskite lattice for efficient production of hydrogen peroxide. *Matter.* 2024;7(6):2265-2277.
38. Seitz LC, Dickens CF, Nishio K, et al. A highly active and stable IrO<sub>x</sub>/SrIrO<sub>3</sub> catalyst for the oxygen evolution reaction. *Science.* 2016;353(6303):1011-1014.
39. Masud J, Umapathi S, Ashokaan N, Nath M. Iron phosphide nanoparticles as an efficient electrocatalyst for the OER in alkaline solution. *J Mater Chem A.* 2016;4(25):9750-9754.
40. Zhang B, Jiang K, Wang H, Hu S. Fluoride-induced dynamic surface self-reconstruction produces unexpectedly efficient oxygen-evolution catalyst. *Nano Lett.* 2018;19(1):530-537.
41. Guan D, Ryu G, Hu Z, et al. Utilizing ion leaching effects for achieving high oxygen-evolving performance on hybrid nanocomposite with self-optimized behaviors. *Nat Commun.* 2020;11(1):3376.
42. Zhang G, Zeng J, Yin J, et al. Iron-facilitated surface reconstruction to in-situ generate nickel-iron oxyhydroxide on self-supported FeNi alloy fiber paper for efficient oxygen evolution reaction. *Appl Catal Environ.* 2021;286:119902.
43. Qiu Z, Ma Y, Edvinsson T. In operando Raman investigation of Fe doping influence on catalytic NiO intermediates for enhanced overall water splitting. *Nano Energy.* 2019;66:104118.
44. Shi Y, Du W, Zhou W, et al. Unveiling the promotion of surface-adsorbed chalcogenate on the electrocatalytic oxygen evolution reaction. *Angew Chem Int Ed.* 2020;59(50):22470-22474.
45. Chang CJ, Zhu Y, Wang J, et al. In situ x-ray diffraction and x-ray absorption spectroscopy of electrocatalysts for energy conversion reactions. *J Mater Chem A.* 2020;8(37):19079-19112.
46. Abed J, Ahmadi S, Laverdure L, et al. In situ formation of nano Ni-Co oxyhydroxide enables water oxidation electrocatalysts durable at high current densities. *Adv Mater.* 2021;33(45):2103812.
47. Harzandi AM, Shadman S, Nissimagoudar AS, et al. Ruthenium core-shell engineering with nickel single atoms for selective oxygen evolution via nondestructive mechanism. *Adv Energy Mater.* 2021;11(10):2003448.
48. Strickler AL, Higgins D, Jaramillo TF. Crystalline strontium iridate particle catalysts for enhanced oxygen evolution in acid. *ACS Appl Energy Mater.* 2019;2(8):5490-5498.
49. Chung DY, Lopes PP, FBD M, et al. Dynamic stability of active sites in hydr (oxy) oxides for the oxygen evolution reaction. *Nat Energy.* 2020;5(3):222-230.
50. Yang C, Batuk M, Jacquet Q, et al. Revealing pH-dependent activities and surface instabilities for Ni-based electrocatalysts during the oxygen evolution reaction. *ACS Energy Lett.* 2018;3(12):2884-2890.
51. Zhao Q, Yan Z, Chen C, Chen J. Spinel: controlled preparation, oxygen reduction/evolution reaction application, and beyond. *Chem Rev.* 2017;117(15):10121-10211.
52. Liu XM, Cui X, Dastafkan K, et al. Recent advances in spinel-type electrocatalysts for bifunctional oxygen reduction and oxygen evolution reactions. *J Energy Chem.* 2021;53:290-302.
53. Olowoyo JO, Kriek RJ. Recent progress on bimetallic-based spinels as electrocatalysts for the oxygen evolution reaction. *Small.* 2022;18(41):2203125.
54. Xu L, Jiang Q, Xiao Z, et al. Plasma-engraved Co<sub>3</sub>O<sub>4</sub> nanosheets with oxygen vacancies and high surface area for the oxygen evolution reaction. *Angew Chem Int Ed.* 2016;128(17):5363-5367.
55. Wang HY, Hung SF, Chen HY, Chan TS, Chen HM, Liu B. In operando identification of geometrical-site-dependent water oxidation activity of spinel Co<sub>3</sub>O<sub>4</sub>. *J Am Chem Soc.* 2016;138(1):36-39.
56. Quast T, Varhade S, Saddeler S, et al. Single particle nanoelectrochemistry reveals the catalytic oxygen evolution reaction activity of Co<sub>3</sub>O<sub>4</sub> nanocubes. *Angew Chem Int Ed.* 2021;60(43):23444-23450.
57. Chakraborty B, Indra A, Menezes PV, Menezes PW. Improved chemical water oxidation with Zn in the tetrahedral site of

- spinel-type  $\text{ZnCo}_2\text{O}_4$  nanostructure. *Mater Today Chem.* 2020; 15:100226.
58. Wang B, Ye Y, Xu L, et al. Space-confined yolk-shell construction of  $\text{Fe}_3\text{O}_4$  nanoparticles inside N-doped hollow mesoporous carbon spheres as bifunctional electrocatalysts for long-term rechargeable zinc-air batteries. *Adv Funct Mater.* 2020;30(51):2005834.
  59. Ji Q, Kong Y, Tan H, et al. Operando identification of active species and intermediates on sulfide interfaced by  $\text{Fe}_3\text{O}_4$  for ultrastable alkaline oxygen evolution at large current density. *ACS Catal.* 2022;12(8):4318-4326.
  60. Cai M, Liu W, Luo X, et al. Three-dimensional and in situ-activated spinel oxide nanoporous clusters derived from stainless steel for efficient and durable water oxidation. *ACS Appl Mater Interfaces.* 2020;12(12):13971-13981.
  61. Duan Y, Lee JY, Xi S, et al. Anodic oxidation enabled cation leaching for promoting surface reconstruction in water oxidation. *Angew Chem Int Ed.* 2021;60(13):7418-7425.
  62. Luo S, Dai C, Ye Y, et al. Elevated water oxidation by cation leaching enabled tunable surface reconstruction. *Angew Chem Int Ed.* 2024;63:e202402184.
  63. Wu T, Sun Y, Ren X, et al. Reconstruction of thiospinel to active sites and spin channels for water oxidation. *Adv Mater.* 2023;35(2):2207041.
  64. Wu T, Sun S, Song J, et al. Iron-facilitated dynamic active-site generation on spinel  $\text{CoAl}_2\text{O}_4$  with self-termination of surface reconstruction for water oxidation. *Nat Catal.* 2019;2(9):763-772.
  65. Chen G, Zhou W, Guan D, et al. Two orders of magnitude enhancement in oxygen evolution reactivity on amorphous  $\text{Ba}_{0.5}\text{Sr}_{0.5}\text{Co}_{0.8}\text{Fe}_{0.2}\text{O}_{3-\delta}$  nanofilms with tunable oxidation state. *Sci Adv.* 2017;3(6):e1603206.
  66. Chen G, Hu Z, Zhu Y, et al. Ultrahigh-performance tungsten-doped perovskites for the oxygen evolution reaction. *J Mater Chem A.* 2018;6(21):9854-9859.
  67. Sun H, Chen G, Sunarso J, Dai J, Zhou W, Shao Z. Molybdenum and niobium codoped B-site-ordered double perovskite catalyst for efficient oxygen evolution reaction. *ACS Appl Mater Interfaces.* 2018;10(20):16939-16942.
  68. May KJ, Carlton CE, Stoerzinger KA, et al. Influence of oxygen evolution during water oxidation on the surface of perovskite oxide catalysts. *J Phys Chem Lett.* 2012;3(22):3264-3270.
  69. Fabbri E, Nachttegaal M, Binninger T, et al. Dynamic surface self-reconstruction is the key of highly active perovskite nanoelectrocatalysts for water splitting. *Nat Mater.* 2017;16(9):925-931.
  70. Sun Y, Li R, Chen X, et al. A-site management prompts the dynamic reconstructed active phase of perovskite oxide OER catalysts. *Adv Energy Mater.* 2021;11(12):2003755.
  71. Geiger S, Kasian O, Ledendecker M, et al. The stability number as a metric for electrocatalyst stability benchmarking. *Nat Catal.* 2018;1(7):508-515.
  72. Chen Y, Sun Y, Wang M, et al. Lattice site-dependent metal leaching in perovskites toward a honeycomb-like water oxidation catalyst. *Sci Adv.* 2021;7(50):eabk1788.
  73. Hubert MA, Patel AM, Gallo A, et al. Acidic oxygen evolution reaction activity-stability relationships in Ru-based pyrochlores. *ACS Catal.* 2020;10(20):12182-12196.
  74. Lebedev D, Povia M, Waltar K, et al. Highly active and stable iridium pyrochlores for oxygen evolution reaction. *Chem Mater.* 2017;29(12):5182-5191.
  75. Zhang N, Wang C, Chen J, et al. Metal substitution steering electron correlations in pyrochlore ruthenates for efficient acidic water oxidation. *ACS Nano.* 2021;15(5):8537-8548.
  76. Lu L, Zheng Z, Yang R, Kakimov A, Li X. Recent advances of layered double hydroxides-based bifunctional electrocatalysts for ORR and OER. *Mater Today Chem.* 2021;21:100488.
  77. Song F, Hu X. Ultrathin cobalt-manganese layered double hydroxide is an efficient oxygen evolution catalyst. *J Am Chem Soc.* 2014;136(47):16481-16484.
  78. Ede SR, Bijoy TK, Sankar SS, Murugan P, Kundu S. Rational design of highly efficient perovskite hydroxide for electrocatalytic water oxidation. *Inorg Chem.* 2020;59(7):4816-4824.
  79. Mann DK, Xu J, Mordvinova NE, et al. Electrocatalytic water oxidation over  $\text{AlFe}_2\text{B}_2$ . *Chem Sci.* 2019;10(9):2796-2804.
  80. Sun Y, Xia Y, Kuai L, et al. Defect-driven enhancement of electrochemical oxygen evolution on Fe-Co-Al ternary hydroxides. *Chem Sus Chem.* 2019;12(12):2564-2569.
  81. Wang J, Kim SJ, Liu J, et al. Redirecting dynamic surface restructuring of a layered transition metal oxide catalyst for superior water oxidation. *Nat Catal.* 2021;4(3):212-222.
  82. Walter C, Menezes PW, Driess M. Perspective on intermetallics towards efficient electrocatalytic water-splitting. *Chem Sci.* 2021;12(25):8603-8631.
  83. Wang K, Huang J, Chen H, et al. Recent progress in high entropy alloys for electrocatalysts. *Electrochem Energy Rev.* 2022;5(S1):17.
  84. Pi Y, Shao Q, Zhu X, Huang X. Dynamic structure evolution of composition segregated iridium-nickel rhombic dodecahedra toward efficient oxygen evolution electrocatalysis. *ACS Nano.* 2018;12(7):7371-7379.
  85. Lee WH, Yi J, Nong HN, et al. Electroactivation-induced IrNi nanoparticles under different pH conditions for neutral water oxidation. *Nanoscale.* 2020;12(27):14903-14910.
  86. Wang L, Saveleva VA, Zafeirotas S, et al. Highly active anode electrocatalysts derived from electrochemical leaching of Ru from metallic  $\text{Ir}_{0.7}\text{Ru}_{0.3}$  for proton exchange membrane electrolyzers. *Nano Energy.* 2017;3(34):385-391.
  87. Xiao W, Lei W, Gong M, Xin HL, Wang D. Recent advances of structurally ordered intermetallic nanoparticles for electrocatalysis. *ACS Catal.* 2018;8(4):3237-3256.
  88. Meng G, Sun W, Mon AA, et al. Strain regulation to optimize the acidic water oxidation performance of atomic-layer IrOx. *Adv Mater.* 2019;31(37):1903616.
  89. Antonyshyn I, Barrios Jiménez AM, Sichevych O, et al.  $\text{Al}_2\text{Pt}$  for oxygen evolution in water splitting: a strategy for creating multifunctionality in electrocatalysis. *Angew Chem Int Ed.* 2020;59(38):16770-16776.
  90. Jiménez AMB, Ormeci A, Burkhardt U, et al. Intermetallic compounds  $\text{M}_2\text{Pt}$  ( $\text{M} = \text{Al, Ga, In, Sn}$ ) in the oxygen evolution reaction. *Sustain Energy Fuels.* 2021;5(22):5762-5772.
  91. Li N, Liu J, Dong BX, Lan YQ. Polyoxometalate-based compounds for photo-and electrocatalytic applications. *Angew Chem Int Ed.* 2020;59(47):20779-20793.
  92. Liu X, Xia F, Guo R, et al. Ligand and anion co-leaching induced complete reconstruction of polyoxomolybdate-organic complex oxygen-evolving pre-catalysts. *Adv Funct Mater.* 2021;31(31):2101792.

93. Wang Y, Zhu Y, Zhao S, et al. Anion etching for accessing rapid and deep self-reconstruction of precatalysts for water oxidation. *Matter*. 2020;3(6):2124-2137.
94. Liu X, Meng J, Ni K, et al. Complete reconstruction of hydrate pre-catalysts for ultrastable water electrolysis in industrial-concentration alkali media. *Cell Rep Phys Sci*. 2020;1(11):100241.
95. Li Y, Wang H, Xie L, Liang Y, Hong G, Dai H. MoS<sub>2</sub> nanoparticles grown on graphene: an advanced catalyst for the hydrogen evolution reaction. *J Am Chem Soc*. 2011;133(19):7296-7299.
96. Zhao J, Wang J, Chen Z, Ju J, Han X, Deng Y. Metal chalcogenides: an emerging material for electrocatalysis. *APL Mater*. 2021;9(5):050902.
97. Peng L, Shah SSA, Wei Z. Recent developments in metal phosphide and sulfide electrocatalysts for oxygen evolution reaction. *Chinese J Catal*. 2018;39(10):1575-1593.
98. Zhang H, Maijenburg AW, Li X, Schweizer SL, Wehrspohn RB. Bifunctional heterostructured transition metal phosphides for efficient electrochemical water splitting. *Adv Funct Mater*. 2020;30(34):2003261.
99. Liu C, Mei B, Shi Z, et al. Operando formation of highly efficient electrocatalysts induced by heteroatom leaching. *Nat Commun*. 2024;15(1):242.
100. Beltrán-Suito R, Forstner V, Hausmann JN, et al. A soft molecular 2Fe-2As precursor approach to the synthesis of nanostructured FeAs for efficient electrocatalytic water oxidation. *Chem Sci*. 2020;11(43):11834-11842.
101. Jiang H, He Q, Li X, et al. Tracking structural self-reconstruction and identifying true active sites toward cobalt oxychloride precatalyst of oxygen evolution reaction. *Adv Mater*. 2019;31(8):1805127.
102. Zhang R, van Straaten G, di Palma V, et al. Electrochemical activation of atomic layer-deposited cobalt phosphate electrocatalysts for water oxidation. *ACS Catal*. 2021;11(5):2774-2785.
103. Mabayoje O, Shoola A, Wygant BR, Mullins CB. The role of anions in metal chalcogenide oxygen evolution catalysis: electrodeposited thin films of nickel sulfide as "pre-catalysts". *ACS Energy Lett*. 2016;1(11):195-201.
104. Zhong C, Han Z, Wang T, et al. Aliovalent fluorine doping and anodization-induced amorphization enable bifunctional catalysts for efficient water splitting. *J Mater Chem A*. 2020;8(21):10831-10838.
105. Wilde P, Dieckhöfer S, Quast T, et al. Insights into the formation, chemical stability, and activity of transient Ni<sub>2</sub>P@NiO<sub>x</sub> core-shell heterostructures for the oxygen evolution reaction. *ACS Appl Energy Mater*. 2020;3(3):2304-2309.
106. Hausmann JN, Mebs S, Laun K, et al. Understanding the formation of bulk-and surface-active layered (oxy) hydroxides for water oxidation starting from a cobalt selenite precursor. *Energ Environ Sci*. 2020;13(10):3607-3619.
107. Siwal SS, Yang W, Zhang Q. Recent progress of precious-metal-free electrocatalysts for efficient water oxidation in acidic media. *J Energy Chem*. 2020;51:113-133.
108. Corrigan DA. The catalysis of the oxygen evolution reaction by iron impurities in thin film nickel oxide electrodes. *J Electrochem Soc*. 1987;134(2):377-384.
109. Hunter BM, Thompson NB, Müller AM, et al. Trapping an iron (VI) water-splitting intermediate in nonaqueous media. *Joule*. 2018;2(4):747-763.
110. Zou S, Burke MS, Kast MG, Fan J, Danilovic N, Boettcher SW. Fe (oxy) hydroxide oxygen evolution reaction electrocatalysis: intrinsic activity and the roles of electrical conductivity, substrate, and dissolution. *Chem Mater*. 2015;27(23):8011-8020.
111. Feng C, Wang F, Liu Z, et al. A self-healing catalyst for electrocatalytic and photoelectrochemical oxygen evolution in highly alkaline conditions. *Nat Commun*. 2021;12(1):5980.
112. Lopes PP, Chung DY, Rui X, et al. Dynamically stable active sites from surface evolution of perovskite materials during the oxygen evolution reaction. *J Am Chem Soc*. 2021;143(7):2741-2750.
113. Zhang R, Dubouis N, Osman MB, et al. A dissolution/precipitation equilibrium on the surface of iridium-based perovskites controls their activity as oxygen evolution reaction catalysts in acidic media. *Angew Chem Int Ed*. 2019;131(14):4619-4623.
114. Li A, Kong S, Adachi K, et al. Atomically dispersed hexavalent iridium oxide from MnO<sub>2</sub> reduction for oxygen evolution catalysis. *Science*. 2024;384(6696):666-670.
115. Chen D, Yu R, Yu K, et al. Bicontinuous RuO<sub>2</sub> nanoreactors for acidic water oxidation. *Nat Commun*. 2024;15(1):3928.
116. Wu ZY, Chen FY, Li B, et al. Non-iridium-based electrocatalyst for durable acidic oxygen evolution reaction in proton exchange membrane water electrolysis. *Nat Mater*. 2023;22(1):100-108.
117. Li J, Wang Y, Zhou T, et al. Nanoparticle superlattices as efficient bifunctional electrocatalysts for water splitting. *J Am Chem Soc*. 2015;137(45):14305-14312.
118. Lai J, Li S, Wu F, Saqib M, Luque R, Xu G. Unprecedented metal-free 3D porous carbonaceous electrodes for full water splitting. *Energ Environ Sci*. 2016;9(4):1210-1214.
119. Oh HS, Nong HN, Reier T, et al. Electrochemical catalyst-support effects and their stabilizing role for IrO<sub>x</sub> nanoparticle catalysts during the oxygen evolution reaction. *J Am Chem Soc*. 2016;138(138):12552-12563.
120. Yan N, Detz RJ, Govindarajan N, et al. Selective surface functionalization generating site-isolated Ir on a MnO<sub>x</sub>/N-doped carbon composite for robust electrocatalytic water oxidation. *J Mater Chem A*. 2019;7(40):23098-23104.
121. Luo F, Hu H, Zhao X, et al. Robust and stable acidic overall water splitting on Ir single atoms. *Nano Lett*. 2020;20(3):2120-2128.
122. Li R, Wang H, Hu F, et al. IrW nanochannel support enabling ultrastable electrocatalytic oxygen evolution at 2 A cm<sup>-2</sup> in acidic media. *Nat Commun*. 2021;12(1):3540.
123. Danilovic N, Subbaraman R, Chang KC, et al. Using surface segregation to design stable Ru-Ir oxides for the oxygen evolution reaction in acidic environments. *Angew Chem Int Ed*. 2014;53(51):14016-14021.
124. Yang L, Yu G, Ai X, et al. Efficient oxygen evolution electrocatalysis in acid by a perovskite with face-sharing IrO<sub>6</sub> octahedral dimers. *Nat Commun*. 2018;9(1):5236.
125. Wu D, Kusada K, Yoshioka S, et al. Efficient overall water splitting in acid with anisotropic metal nanosheets. *Nat Commun*. 2021;12(1):1145.



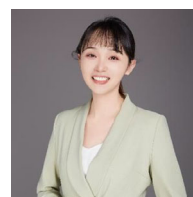
126. Zhu Y, Guo C, Zheng Y, Qiao SZ. Surface and interface engineering of noble-metal-free electrocatalysts for efficient energy conversion processes. *Acc Chem Res.* 2017;50(4):915-923.
127. Kwon T, Jun M, Joo J, Lee K. Nanoscale hetero-interfaces between metals and metal compounds for electrocatalytic applications. *J Mater Chem A.* 2019;7(10):5090-5110.
128. Yao Y, Hu S, Chen W, et al. Engineering the electronic structure of single atom Ru sites via compressive strain boosts acidic water oxidation electrocatalysis. *Nat Catal.* 2019;2(4):304-313.
129. Shan J, Guo C, Zhu Y, et al. Charge-redistribution-enhanced nanocrystalline Ru@ IrOx electrocatalysts for oxygen evolution in acidic media. *Chem.* 2019;5(2):445-459.
130. Cui X, Ren P, Ma C, et al. Robust interface Ru centers for high-performance acidic oxygen evolution. *Adv Mater.* 2020;32(25):1908126.
131. Wen Y, Chen P, Wang L, et al. Stabilizing highly active Ru sites by suppressing lattice oxygen participation in acidic water oxidation. *J Am Chem Soc.* 2021;143(17):6482-6490.

## AUTHOR BIOGRAPHIES

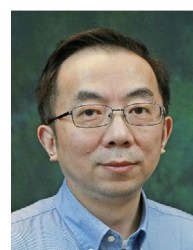


**Gao Chen** works in the School of Chemistry and Materials Science, Nanjing University of Information Science and Technology (NUIST). After obtaining his PhD degree, he received postdoc training at Nanyang Technology University and The Hong Kong Polytechnic University. His primary research interest is elucidating the fundamental connections between materials and reaction mechanisms in electrocatalysis. Additionally, he focuses on

developing integrated systems for seawater purification and splitting to produce green hydrogen.



**Yanping Zhu** received her PhD in Chemical Engineering from Nanjing Tech University. From 2018 to 2023, she worked as a postdoctoral fellow at National Taiwan University and The Hong Kong Polytechnic University. Since 2024, she has joined the college of materials science and technology at Nanjing University of Aeronautics and Astronautics. Her research interests include developing advanced materials related to electrocatalysis and in situ methodologies toward various chemical reactions.



**Haitao Huang** is a Tenured Professor in the Department of Applied Physics at The Hong Kong Polytechnic University. His research interests cover the synthesis, characterization, and investigation of the physical mechanisms underlying dielectric materials, as well as new low-dimensional nanostructured materials for energy applications. He is currently a Fellow of the Royal Society of Chemistry.

**How to cite this article:** Chen G, Zhu Y, She S, Lin Z, Sun H, Huang H. Component leaching of water oxidation electrocatalysts. *InfoMat.* 2024; 6(11):e12609. doi:[10.1002/inf2.12609](https://doi.org/10.1002/inf2.12609)